The Astrophysical Journal Supplement Series, 273:12 (16pp), 2024 July https://doi.org/10.3847/1538-4365/ad4a6f

Candidate Members of the VMP/EMP Disk System of the Galaxy from the SkyMapper and SAGES Surveys

Jihye Hong[1,2], Timothy C. Beers[1,2], Young Sun Lee[1,3], Yang Huang[4,5], Yutaka Hirai[1,2,6,11], Jonathan Cabrera Garcia[1,2], Derek Shank[1,2], Shuai Xu[7,8], Haibo Yuan[7,8], Mohammad K. Mardini[9,10], Thomas Catapano[1,2], Gang Zhao[5], Zhou Fan[5], Jie Zheng[5], Wei Wang[5], Kefeng Tan[5], Jingkun Zhao[5], and Chun Li[5]

[1] Department of Physics and Astronomy, University of Notre Dame, Notre Dame, IN 46556, USA
[2] Joint Institute for Nuclear Astrophysics—Center for the Evolution of the Elements (JINA-CEE), USA
[3] Department of Astronomy and Space Science, Chungnam National University, Daejeon 34134, Republic of Korea
[4] School of Astronomy and Space Science, University of Chinese Academy of Sciences, Beijing 100049, People's Republic of China
[5] CAS Key Lab of Optical Astronomy, National Astronomical Observatories, Chinese Academy of Sciences, Beijing 100101, People's Republic of China
[6] Astronomical Institute, Tohoku University, 6-3 Aoba, Aramaki, Aoba-ku, Sendai, Miyagi 980-8578, Japan
[7] Institute for Frontiers in Astronomy and Astrophysics, Beijing Normal University, Beijing 102206, People's Republic of China
[8] Department of Astronomy, Beijing Normal University, Beijing, 100875, People's Republic of China
[9] Department of Physics, Zarqa University, Zarqa 13110, Jordan
[10] Jordanian Astronomical Virtual Observatory, Zarqa University, Zarqa 13110, Jordan
Received 2023 November 2; revised 2024 April 17; accepted 2024 April 18; published 2024 July 8

Abstract

Photometric stellar surveys now cover a large fraction of the sky, probe to fainter magnitudes than large-scale spectroscopic surveys, and are relatively free from the target selection biases often associated with such studies. Photometric-metallicity estimates that include narrow/medium-band filters can achieve comparable accuracy and precision to existing low-resolution spectroscopic surveys such as Sloan Digital Sky Survey/SEGUE and LAMOST. Here we report on an effort to identify likely members of the Galactic disk system among the very metal-poor (VMP; [Fe/H] $\leqslant -2$) and extremely metal-poor (EMP; [Fe/H] $\leqslant -3$) stars. Our analysis is based on an initial sample of ∼11.5 million stars with full space motions selected from the SkyMapper Southern Survey (SMSS) and Stellar Abundance and Galactic Evolution Survey (SAGES). After applying a number of quality cuts to obtain the best available metallicity and dynamical estimates, we analyze a total of ∼5.86 million stars in the combined SMSS/SAGES sample. We employ two techniques that, depending on the method, identify between 876 and 1476 VMP stars (6.9%−11.7% of all VMP stars) and between 40 and 59 EMP stars (12.4%−18.3% of all EMP stars) that appear to be members of the Galactic disk system on highly prograde orbits ($v_\phi > 150\,\mathrm{km\,s^{-1}}$). The total number of candidate VMP/EMP disklike stars is 1496, the majority of which have low orbital eccentricities, ecc $\leqslant 0.4$; many have ecc $\leqslant 0.2$. The large fractions of VMP/EMP stars associated with the Milky Way disk system strongly suggest the presence of an early-forming "primordial" disk.

Unified Astronomy Thesaurus concepts: Milky Way Galaxy (1054); Milky Way dynamics (1051); Milky Way disk (1050); Milky Way evolution (1052); Milky Way formation (1053); Galactic archaeology (2178)

Supporting material: machine-readable tables

1. Introduction

Over the past few decades, large-scale spectroscopic surveys, such as the HK Survey (Beers et al. 1985, 1992), the Hamburg/ESO Survey (Christlieb 2003), the Sloan Digital Sky Survey (SDSS; York et al. 2000), SEGUE (Yanny et al. 2009; Rockosi et al. 2022), RAVE (Steinmetz et al. 2006), LAMOST (Deng et al. 2012; Zhao et al. 2012), GALAH (De Silva et al. 2015), APOGEE (Majewski et al. 2017), the H3 Survey (Conroy et al. 2019), the Gaia-ESO survey (Gilmore et al. 2022), and the Gaia mission (Gaia Collaboration et al. 2023), have changed the paradigm of observational studies by providing detailed chemical and kinematic information for numerous stars in the Milky Way (MW), in particular for the relatively rare very metal-poor (VMP; [Fe/H] $\leqslant -2$) and extremely metal-poor (EMP; [Fe/H] $\leqslant -3$) stars.

In a series of recent papers, An & Beers (2020, 2021a, 2021b) and An et al. (2023) have constructed "blueprints" of the MW's stellar populations from analyses of the orbital rotation (inferred from proper motions and distance estimates alone) as a function of carefully calibrated photometric-metallicity estimates for stars with available broadband *ugriz* from SDSS/SEGUE and other surveys. This approach has proven quite powerful. Among other results, these authors not only identified previously known substructures and confirmed the presence of the inner- and outer-halo populations but also demonstrated that the metal-weak thick disk (MWTD; Norris et al. 1985; Carollo et al. 2007, 2010; Beers et al. 2014) is a separable population with lower metallicity and rotation that lags the canonical thick disk, as shown in Carollo et al. (2019). In addition, they identified a continuous sequence of stars in the rotational velocity versus metallicity space that may be associated with a starburst event when the earlier disk system encountered Gaia−Sausage−Enceladus (GSE;

[11] JSPS Research Fellow.

Belokurov et al. 2018; Haywood et al. 2018; Helmi et al. 2018). Evidence for this starburst event is also reported in Lee et al. (2023).

Whether surveys to identify likely metal-poor (MP) stars are performed with fiber-fed spectrographs such as SDSS or LAMOST or broadband photometric efforts such as SEGUE or Pan-STARRS (Chambers et al. 2016), it is challenging to avoid target selection biases that can confound the relative contributions of stars with different metallicity to the recognized Galactic components. In addition, the first step in surveys dedicated to finding low-metallicity stars is often to limit the regions of the sky under consideration to higher Galactic latitude (e.g., $|b| > 30°$), precluding identification of substantial numbers of VMP/EMP stars in the disk system of the MW.

Nonetheless, recent papers have provided identifications of VMP/EMP (and a handful of ultra-MP, [Fe/H] $\leqslant -4$) stars in the MW with disklike orbits, based on medium-resolution and, in some cases, high-resolution spectroscopic follow-up (see, e.g., Schlaufman et al. 2018; Sestito et al. 2019, 2020; Di Matteo et al. 2020; Venn et al. 2020; Carter et al. 2021; Cordoni et al. 2021; Fernández-Alvar et al. 2021; Limberg et al. 2021; Mardini et al. 2022a, 2022b; Carollo et al. 2023; Mardini et al. 2024, and references therein).

Over the past few years, photometric surveys based on combinations of narrowband and medium- to broadband filters have been (or are being) executed (e.g., SkyMapper, Keller et al. 2007; the Pristine Survey, Starkenburg et al. 2017; Stellar Abundance and Galactic Evolution Survey (SAGES), Zheng et al. 2018, Cenarro et al. 2019; J-PLUS, Mendes de Oliveira et al. 2019; S-PLUS). Typically, such surveys do not avoid regions of the MW at lower Galactic latitudes, other than those limited by very high interstellar extinction and reddening or crowding. As a result, VMP/EMP stars in the MW's disk system have been increasingly discovered, though their numbers are still relatively small.

The SkyMapper Southern Survey Data Release 2 (SMSS DR2; Onken et al. 2019) was carefully recalibrated by Huang et al. (2021) and used by Huang et al. (2022) to derive stellar parameters, luminosity classifications, and metallicity estimates for over 24 million stars in the Southern Hemisphere. These authors derived effective temperatures ($T_{\rm eff}$) by adopting metallicity-dependent $T_{\rm eff}$–color relations constructed from Gaia $(G_{\rm BP} - G_{\rm RP})_0$, LAMOST $T_{\rm eff}$, and [Fe/H]. The effective temperature scale of LAMOST has been shown to agree with that of direct measurements (Huang et al. 2015). They adopted Bayesian distance estimates (Bailer-Jones et al. 2021) and ages from the PAdova and tRieste Stellar Evolutionary Code (PARSEC; Bressan et al. 2012; Marigo et al. 2017) isochrones. In addition, an empirical metallicity-dependent stellar-locus method (Yuan et al. 2015) was used to estimate the photometric metallicity, with combinations of the SMSS narrow/medium u- and v-band filter magnitudes, the $G_{\rm BP}$ magnitude from the Gaia ultra-wide-band prism spectra, and a maximum likelihood approach (Huang et al. 2022).

The recently completed SAGES (Fan et al. 2023), which employs similar, but not identical, filters to SMSS, has been employed by Huang et al. (2023) to obtain stellar parameters, luminosity classifications, and metallicity estimates for nearly 26 million stars in the Northern Hemisphere.

Here we identify 1496 VMP and 61 EMP candidate stars with disklike orbits populating the rapidly rotating disk system of the MW ($v_\phi > 150\,{\rm km\,s^{-1}}$), selected from a subset of roughly 11.5 million stars from the SMSS and SAGES photometric surveys with available radial velocities (RVs), proper motions, and other astrometric data from which full space motions are derived. We approximately separate stars with disklike orbits from stars with halo-like orbits by two criteria that have been commonly used in the literature (Haywood et al. 2018; Di Matteo et al. 2020; Mardini et al. 2022a; Bellazzini et al. 2024) and then consider their relative fractions at low metallicities.

This paper is organized as follows: In Section 2, we describe the data sets we employ and the choices made for the adopted metallicity estimates, as well as the derivation of dynamical parameters. In this section we also describe two methods that have been commonly used to identify stars with potential disklike orbits. In Section 3, we present maps of the orbital rotational velocities of the stars as a function of [Fe/H], where potential VMP/EMP candidates with disklike orbits can already be seen, and compare their relative fractions as a function of [Fe/H]. In Section 4, we present a discussion, along with conjectures on the origins of VMP/EMP disklike stars based on interpretations from numerical simulations. We conclude with a summary and future prospects in Section 5.

2. Data and Methods

2.1. Data

Huang et al. (2022) derived stellar parameters, including metallicity estimates, for more than 19 million dwarfs and 5 million giants over essentially the entire Southern Hemisphere from SMSS DR2, including about 731,000 VMP and 27,000 EMP stars. If we restrict their sample to stars with available RVs from Gaia DR3 (Gaia Collaboration et al. 2023) and other sources, the number of stars is about 7.4 million, including roughly 56,000 VMP and 2300 EMP stars.

SAGES observed slightly less than half of the Northern Hemisphere. Notably, SAGES did not cover a large fraction of the north Galactic pole (NGP), while SMSS covered the entire south Galactic pole (SGP). Another crucial difference between SAGES and SMSS is that the central wavelength of the SAGES v-band filter is shifted redward relative to the SMSS v-band filter by about 110 Å, so it fully includes the region of the Ca II H and K lines (Zheng et al. 2018). Huang et al. (2023) used a similar approach to Huang et al. (2022) and obtained effective temperatures, luminosity classifications based on surface gravity, and metallicity estimates for over 26 million stars, including some 874,000 VMP and 13,000 EMP stars from SAGES DR1 (Fan et al. 2023). About 4.1 million stars in this catalog have available RVs, including roughly 41,000 VMP and 1900 EMP stars.

For this study, we begin with a sample of about 7.4 million stars from SMSS and 4.1 million stars from SAGES with available RVs, proper motions, and distance estimates, as provided in the catalogs from Huang et al. (2022) and Huang et al. (2023), respectively. After combining these data sets, binary stars photometrically classified by Huang et al. (2022, 2023) and cool dwarfs ($T_{\rm eff} < 4500\,{\rm K}$) have been removed. We have additionally applied a more restrictive cut on the bp_rp_excess_factor, $< 0.12 \times ({\rm BP}-{\rm RP})_0 + 1.13/1.14$ cuts for dwarfs/giants, respectively, as in Xu et al. (2022), and on the renormalized unit weight error (RUWE) < 1.1, in order to exclude possible binary stars. Cuts based on an empirical isochrone, similar to the PARSEC (Bressan et al. 2012;

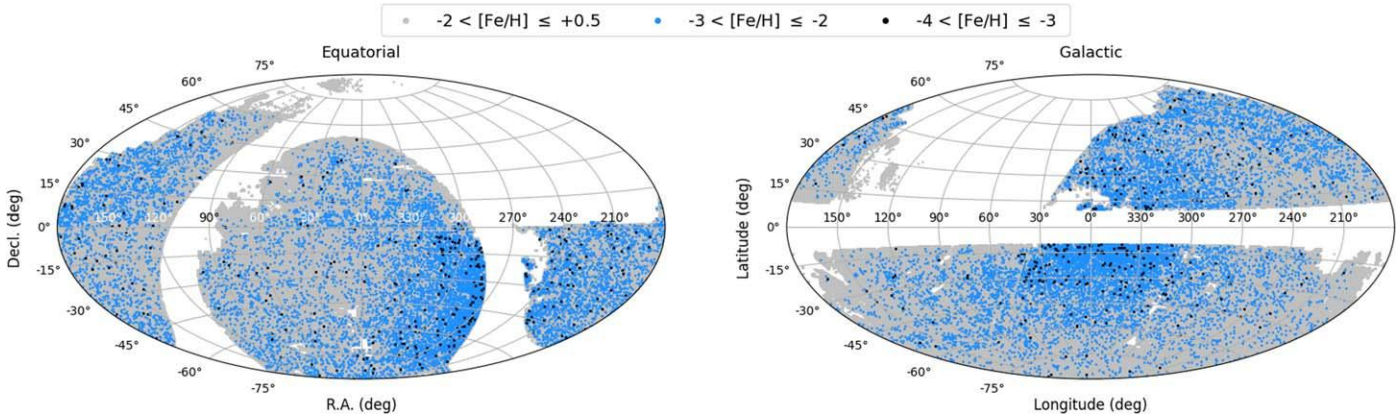

Figure 1. Mollweide projection of the positions for 5.86 million stars selected from the Southern Hemisphere (SMSS) and Northern Hemisphere (SAGES) photometric surveys, in equatorial (left panel) and Galactic (right panel) coordinates. The metallicity of this final sample is based on calibrated $v - G_{BP}$ colors and a combination of the u/v bands from SMSS/SAGES (Huang et al. 2022, 2023). See the Appendix for a discussion of the cuts that are applied to the sample prior to assigning the final metallicities. The gray filled circles indicate the stars with derived metallicities in the range $-2 < [Fe/H] \leqslant +0.5$, the light-blue filled circles are stars with $-3 < [Fe/H] \leqslant -2$, and the black filled circles represent stars with $-4 < [Fe/H] \leqslant -3$. The stars shown all have available RVs and astrometric information. For the purpose of our analysis, we exclude stars identified as likely binaries by Huang et al. (2022, 2023), cool dwarfs ($T_{eff} < 4500$ K), metal-rich stars masquerading as VMP/EMP stars (see text), and likely members of recognized globular clusters. For stars in common between the two surveys, we have used the average value of the photometric-metallicity estimates.

Marigo et al. 2017) isochrone with [Fe/H] = −2 at age = 12 Gyr, were also applied to eliminate the significant contamination from metal-rich stars that could masquerade as VMP/EMP stars. These restrictions removed a total of about 3.3 million stars.

Moreover, we removed about 940 likely stellar globular cluster members based on the catalogs of Harris (2010)[12] and Baumgardt & Vasiliev (2021). Finally, in order to diminish the effect of reddening on the derived metallicities (of particular importance for stars near the disk), we only included stars with $E(B-V) \leqslant 0.3$, excluding a total of about 17,000 stars. More discussion about the extinction cut is provided in the Appendix.

Metallicity estimates for the stars in our sample are based on calibrated $u - G_{BP}$ colors and $v - G_{BP}$ colors, a combination of the u/v bands from SMSS/SAGES and the ultra-wide-band Gaia G_{BP} prism spectra (Huang et al. 2022, 2023). As has been noted previously, the colors involving the u band have a greater sensitivity to the presence of enhanced carbon in a star than those involving the v band. For this reason, and in order to provide the best available metallicities, we do not include stars for which only u-band metallicity estimates are available, those that have a difference between the u-band- and v-band-based abundances greater than 0.5 dex, and stars with estimated metallicity errors greater than 0.5 dex. See the Appendix for a justification and full discussion of the cuts that are applied to the sample prior to assigning final adopted metallicities. Note that we refer to the photometric-metallicity estimates as [Fe/H] in this study, unless otherwise indicated.

2.2. Dynamical Parameters

Orbital parameters for the stars in our combined sample are determined using their 6D astrometric parameters (positions, RVs, proper motions, and distance estimates from Huang et al. 2022, 2023), as well as their corresponding errors, as inputs to the Action-based GAlaxy Modelling Architecture[13] (AGAMA) package (Vasiliev 2019), adopting the solar positions and peculiar motions described in Shank et al. (2022),[14] and the gravitational potential MW2017 (McMillan 2017).

Similar to Shank et al. (2022), we input quantities through the orbital integration process in AGAMA to calculate the cylindrical velocities (v_r, v_ϕ, v_z), cylindrical actions (J_r, J_ϕ, J_z), orbital specific energy (E), r_{apo}, r_{peri}, eccentricity (ecc), Z_{max} (the maximum orbital distances reached by stars from the Galactic plane), and R_{max} (the maximum apocentric distance projected onto the Galactic plane), along with their associated errors.[15] Stars that are possibly unbound ($E > 0$ km^2 s^{-2}) were identified and removed. This resulted in a total of 10.8 million from the initial 11.5 million stars that are suitable for our kinematic analysis. For our present purpose, we only included stars having derived errors less than 25 km s^{-1} in their orbital rotation velocities and relative errors $\leqslant$30% in Z_{max} and R_{max}, which removed about 165,000 stars from the combined sample. This produced a final sample of approximately 5.86 million stars, including 4.07 million SMSS and 1.79 million SAGES stars, which we refer to as the SMSS/SAGES sample hereafter.

Figure 1 shows the sky distribution in equatorial and Galactic coordinates for the final 5.86 million stars of the combined SMSS/SAGES sample. The gray filled circles indicate the stars with $-2 < [Fe/H] \leqslant +0.5$, the light-blue filled circles are stars with $-3 < [Fe/H] \leqslant -2$, and the black filled circles represent stars with $-4 < [Fe/H] \leqslant -3$. The ∼143,000 stars in common between the two surveys have

[12] https://physics.mcmaster.ca/~harris/mwgc.dat

[13] http://github.com/GalacticDynamics-Oxford/Agama

[14] We adopt a solar position of (−8.249, 0, 0) kpc (GRAVITY Collaboration et al. 2020) and solar peculiar motion (U, V W), about the local standard of rest (LSR), of (11.1, 12.24, 7.25) km s^{-1} (Schönrich et al. 2010), where $V_{LSR} = 238.5$ km s^{-1}, defined as $V_{LSR} = V_\odot - V$ and $V_\odot = 250.70$ km s^{-1}, determined from Reid & Brunthaler (2020) based on our choice of solar position and using the proper motion of the center of the Galaxy (Sgr A*) of −6.411 mas yr^{-1}.

[15] Due to the very large number of stars in our sample, we estimated errors on R_{max}, unlike for the other dynamical parameters, by running the input quantities and their errors 50 times through AGAMA using a random sample of 10,000 stars, and we assume that the relative errors apply to all stars.

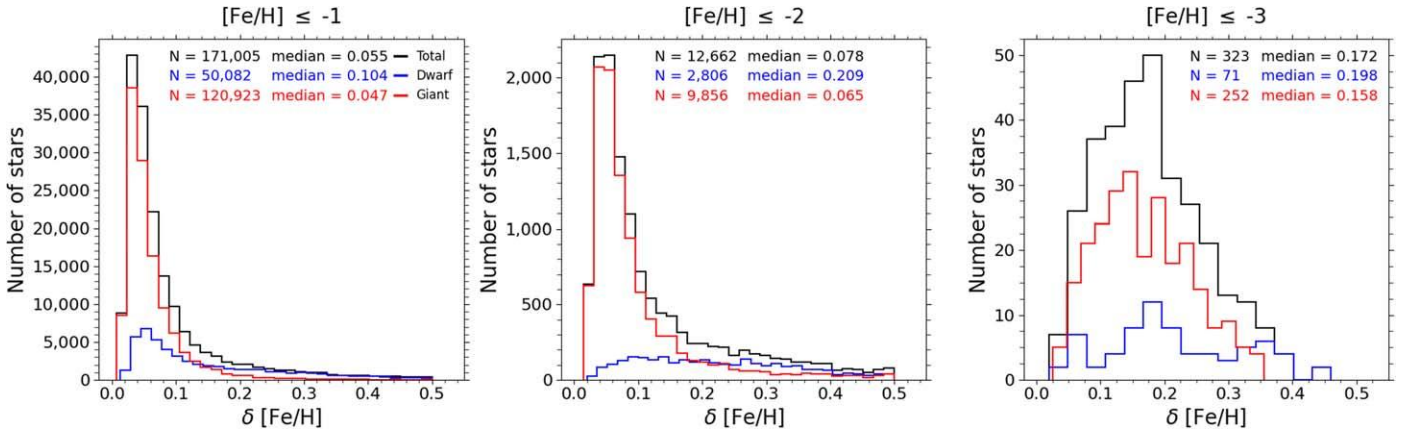

Figure 2. Histogram of the errors in photometric-metallicity estimates (δ [Fe/H]) for the final SMSS/SAGES sample. From left to right, the panels correspond to MP ([Fe/H] $\leqslant -1$), VMP ([Fe/H] $\leqslant -2$), and EMP ([Fe/H] $\leqslant -3$) subsamples, respectively. The black, blue, and red histograms represent the total, dwarf, and giant stars in each metallicity range, respectively. The number of stars and the median values of δ [Fe/H] are indicated in the legend of each panel.

differences in [Fe/H] from the v band with a median value of only 0.02 dex; we have adopted an average of these determinations for these stars.

Figure 2 shows the distribution of the errors in the photometric-metallicity estimates (δ [Fe/H]) for the combined SMSS/SAGES sample. The left, middle, and right panels provide the results for the subsamples of stars with [Fe/H] $\leqslant -1$, -2, and -3, respectively. The legends in each panel indicate the median errors for all stars in the listed metallicity range and the errors for stars classified as dwarfs and giants. As can be seen, the errors increase with decreasing metallicity, as expected, but still remain reasonably low (median errors on the order of 0.1−0.2 dex). Note that the external errors are somewhat larger, on the order of 0.25−0.35 dex (see the discussion in the Appendix).

2.3. Separation of Disk and Halo Stars

Previous analyses of the nature of stellar orbits in the MW have used a variety of techniques to separate stars on disklike orbits from stars on halo-like orbits. Two simple approaches are described below.

2.3.1. Maximum Height of Orbits

This approach, employed by Beers et al. (2014), Sestito et al. (2020, 2021), Limberg et al. (2021), Mardini et al. (2022a), and Bellazzini et al. (2024), identifies stars in the disklike and halo-like dynamical populations by assigning stars with $Z_{\rm max} \leqslant 3$ kpc to disklike orbits and those with $Z_{\rm max} > 3$ kpc to halo-like orbits. Often, an additional criterion is adopted to identify the stars in the disk system by demanding that they be on highly prograde orbits. We follow a similar approach to that described below, with a further division of the stars on disklike orbits into those with $Z_{\rm max} \leqslant 1$ kpc, in an attempt to identify possible VMP/EMP thin-disk stars.

2.3.2. "Wedges" in the Haywood Diagram

Following Haywood et al. (2018), we have also used plots of $Z_{\rm max}$ versus arctan $(Z_{\rm max}/R_{\rm max})$, which redistributes our sample stars into discrete wedges, corresponding to different dynamical populations, a method also employed by Schuster et al. (2012), Di Matteo et al. (2020), Kim et al. (2021), and Koppelman et al. (2021).

Here $R_{\rm max}$ is defined as the projection of $r_{\rm apo}$ onto the Galactic plane, via the simple geometric relationship $R_{\rm max} = \sqrt{r_{\rm apo}^2 - Z_{\rm max}^2}$. Note that, for simplicity of notation, below we define an "inclination angle" (IA) to represent arctan $(Z_{\rm max}/R_{\rm max})$. It should be kept in mind that $Z_{\rm max}$ and $R_{\rm max}$ are derived from the full ensemble of orbits traced by a given star, so their IA is representative of that complete set, not a single orbit or an average of the orbits.

3. Results

In this section, we identify about 12,700 VMP/EMP stars over the full range of the rotational velocities of the final 5.86 million stars in the combined SMSS/SAGES sample. Among these metal-deficient stars, we closely examine the 2150 rapidly rotating VMP/EMP stars, in order to classify them as on halo-like or disklike orbits.

3.1. v_ϕ versus [Fe/H]

Figure 3 shows plots of stellar number density for our sample in the rotational velocity versus photometric-metallicity plane. The top panel indicates the total combined SMSS/SAGES sample color-coded on a logarithmic scale. The rapidly rotating canonical disk system (comprising both the thin disk and thick disk) is most visible for [Fe/H] > -1. In addition, as reported in the series of papers by An & Beers (2020, 2021a, 2021b), the MWTD, the Splashed Disk (SD), and a hint of the GSE substructure can be seen in the black dashed ellipses. However, the VMP/EMP stars in the rapidly rotating disk region ($v_\phi > 150$ km s^{-1}; the average value of rotational velocity for the MWTD from Carollo et al. 2010) are less visible in the number density map than the other components. Thus, we represent the ∼2150 highly prograde VMP/EMP candidates with white circles (out of a total number of about 12,700 VMP/EMP stars). The middle and bottom panels are the same v_ϕ versus [Fe/H] plane, but for dwarfs and giants, respectively. There are about 2800 total VMP/EMP dwarfs and 9900 total VMP/EMP giants. The subsets of these stars with $v_\phi > 150$ km s^{-1} are roughly 650 VMP/EMP dwarfs and 1500 VMP/EMP giants, respectively. We point out that, at this stage, we have not separated the VMP/EMP stars with disklike orbits from those with halo-like orbits. However, from inspection of the middle and bottom panels, it is clear that

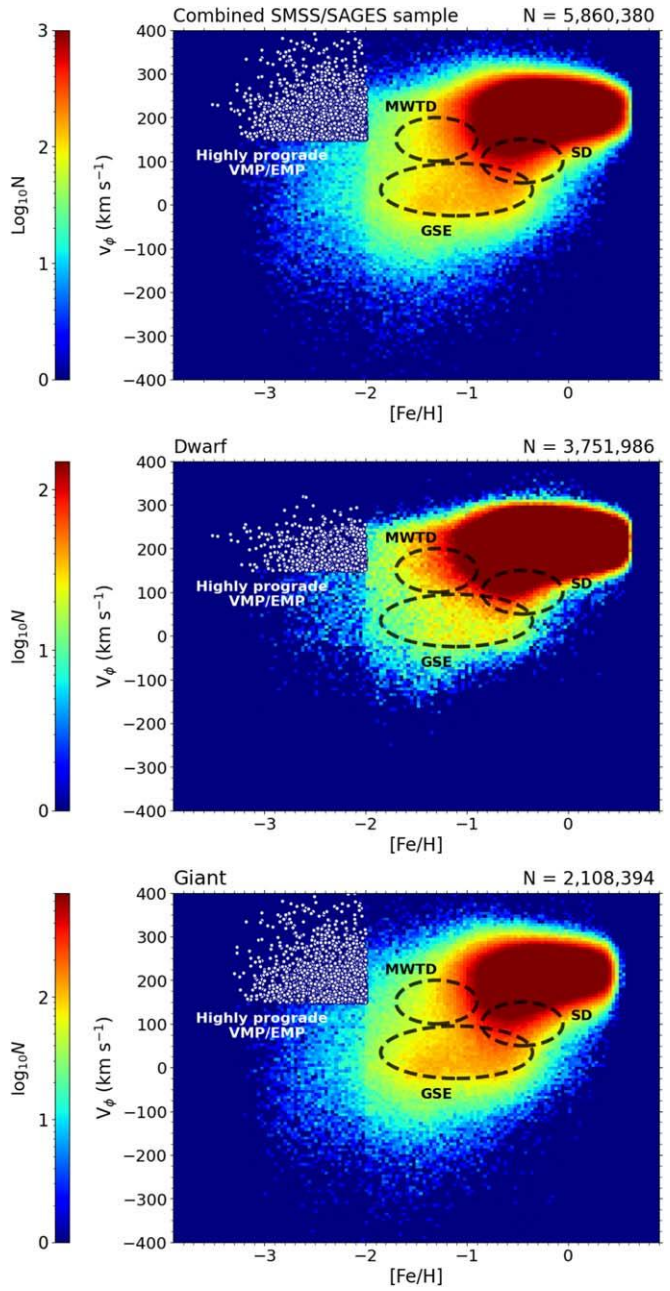

Figure 3. Top panel: rotational velocity distribution (v_ϕ) of the SMSS/SAGES sample as a function of photometric metallicity ([Fe/H]). The number density is color-coded on a logarithmic scale. The MWTD, the SD, and the GSE substructure are marked with black dashed ellipses. The highly prograde VMP/EMP candidates are shown by white circles. Middle panel: same as the top panel, but for dwarfs. Bottom panel: same as the top panel, but for giants. The number of VMP/EMP stars with $v_\phi > 150$ km s^{-1} is about 2150, including 650 dwarfs and 1500 giants.

the distribution of rotational velocity for the VMP/EMP giants (which are expected to contain a greater fraction of halo-like orbits) in the bottom panel stands in contrast to that of the VMP/EMP dwarfs, seen in the middle panel.

3.2. Fractions of Disklike and Halo-like Stars

3.2.1. Based on the $Z_{\rm max}$ Criterion

We first consider MP ([Fe/H] $\leqslant -1$) stars in three regions of $Z_{\rm max}$: $Z_{\rm max} > 3$ kpc, $Z_{\rm max} \leqslant 3$ kpc, and $Z_{\rm max} \leqslant 1$ kpc. We assign the stars with $Z_{\rm max} > 3$ kpc to the halo populations, while those with $Z_{\rm max} \leqslant 3$ kpc and $Z_{\rm max} \leqslant 1$ kpc are candidate members of the MP thick- and thin-disk systems, respectively. The left panel of Figure 4 shows the cumulative numbers of each population. At [Fe/H] $\leqslant -2$, approximately 9600 halo stars with $Z_{\rm max} > 3$ kpc (black line) were found, along with about 3000 stars with $Z_{\rm max} \leqslant 3$ kpc (red line) and 430 stars with $Z_{\rm max} \leqslant 1$ kpc (blue line). The middle panel shows the cumulative distribution function (CDF) for each population, normalized by the number of MP stars. Roughly 11.5% of the MP stars assigned to the halo system are VMP stars, and 0.24% are EMP stars; about 3.5% of the MP stars assigned to the disk system are VMP stars, and 0.08% are EMP stars. It is interesting to note that the CDFs of the stars with $Z_{\rm max} \leqslant 3$ kpc and $Z_{\rm max} \leqslant 1$ kpc are almost identical.

The right panel of Figure 4 shows the distribution of orbital eccentricity for [Fe/H] $\leqslant -1$ of these subsamples split on $Z_{\rm max}$. The broad distribution of eccentricity, peaking at high eccentricity, for stars kinematically assigned to the halo population is clear, as is the presence of low-eccentricity stars among the stars assigned to the disk system. Note that at this point we have not applied any cuts on v_ϕ, only on $Z_{\rm max}$, so we expect that the subsamples of stars with $Z_{\rm max} \leqslant 3$ kpc and $Z_{\rm max} \leqslant 1$ kpc have some level of contamination from halo stars.

Figure 5 shows the distribution of v_ϕ for these three subsamples, but only for stars with [Fe/H] $\leqslant -2$, [Fe/H] $\leqslant -2.5$, and [Fe/H] $\leqslant -3$, from the left to right panels, respectively. The vertical dashed line corresponds to a cut on $v_\phi = 150$ km s^{-1}, the average orbital rotation value for the MWTD from Carollo et al. (2010). We note that the adopted limit for the MWTD stars with the lowest v_ϕ from Carollo et al. (as well as from An & Beers 2021b) is $v_\phi \sim 100$ km s^{-1}. From inspection, there remains considerable contamination of the VMP/EMP stars with prograde disklike orbits by stars with prograde halo-like orbits, even with the higher cut at $v_\phi > 150$ km s^{-1} (although it is substantially less for the EMP stars shown in the right panel), indicating that a more sophisticated separation methodology is desirable.

Figure 6 shows histograms of the eccentricity distribution for stars with [Fe/H] $\leqslant -2$, -2.5, and -3, respectively. We now subdivide the stars into three regions: $Z_{\rm max} > 3$ kpc, 1 kpc $< Z_{\rm max} \leqslant 3$ kpc, and $Z_{\rm max} \leqslant 1$ kpc, in an attempt to better isolate stars with thick-disk orbits from those with thin-disk orbits. We note that these divisions are imperfect, in that we expect there to be contamination from halo stars at all $Z_{\rm max}$. Within the 1 kpc $< Z_{\rm max} \leqslant 3$ kpc region there should be few thin-disk stars. Within the cut $Z_{\rm max} \leqslant 1$ kpc there will also remain some contamination from thick-disk stars.

From inspection of the top row of panels in Figure 6, which includes stars on both retrograde and prograde orbits, the VMP/EMP stars do not exhibit prominent low-eccentricity orbits in all three ranges of [Fe/H]. However, in the bottom row of panels, the introduction of the $v_\phi > 150$ km s^{-1} cut greatly increases the relative dominance of VMP/EMP stars with disklike orbits, including for stars with ecc $\leqslant 0.4$. We note that similar results for VMP stars have been found by Bellazzini et al. (2024), based on a sample of some 700,000 stars with photometric-metallicity estimates obtained with synthetic Strömgren photometry from Gaia DR3 by Bellazzini et al. (2023).

3.2.2. Based on the Haywood Criterion

There is also evidence for the existence of a VMP/EMP disk system from the Haywood diagram. Figure 7 shows the

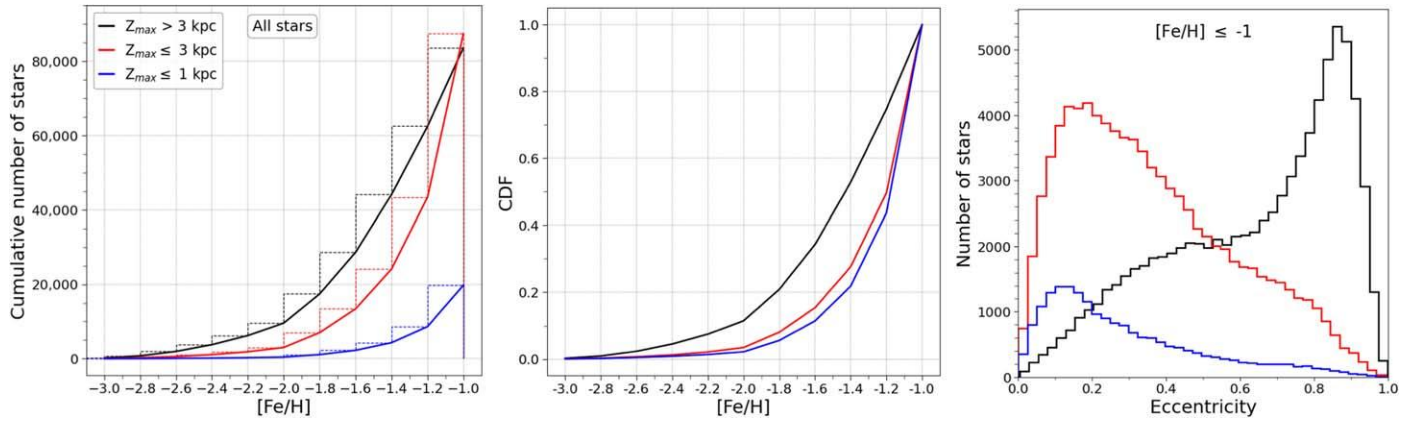

Figure 4. Left panel: cumulative number distribution of the MP ([Fe/H] $\leqslant -1$) stars as a function of [Fe/H], for stars with $Z_{\rm max}$ >3 kpc (black line), $Z_{\rm max}$ $\leqslant$3 kpc (red line), and $Z_{\rm max}$ $\leqslant$1 kpc (blue line). Middle panel: cumulative distribution functions of [Fe/H] for these subsamples. Each population is normalized on the basis of the number of stars at [Fe/H] $= -1$. Right panel: eccentricity distribution for these subsamples with [Fe/H] $\leqslant -1$.

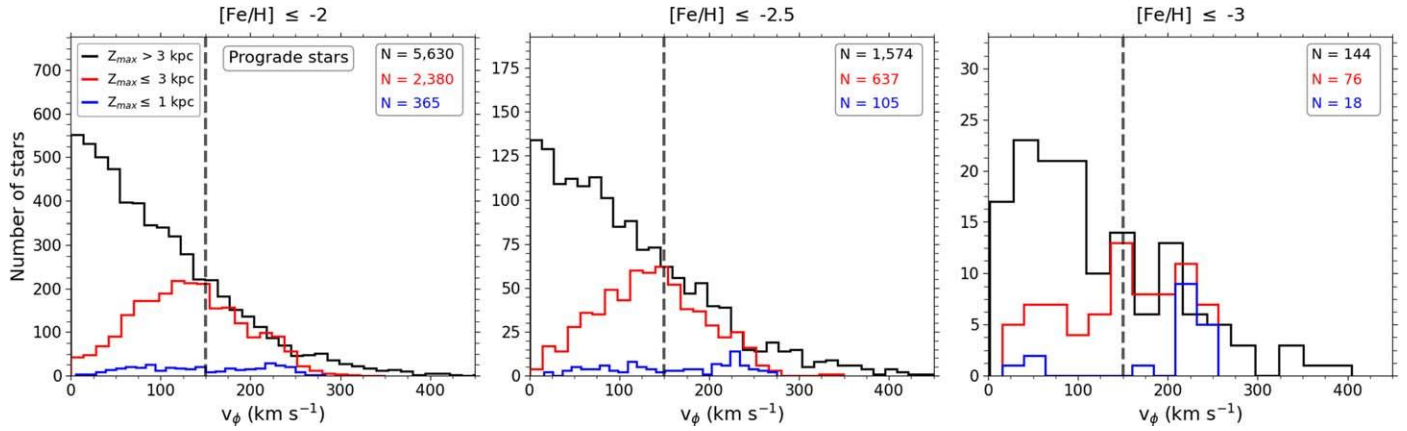

Figure 5. Number distributions of VMP/EMP stars with prograde orbits as a function of rotational velocity (v_ϕ), for the stars with [Fe/H] $\leqslant -2$ (left panel), -2.5 (middle panel), and -3 (right panel), respectively. The vertical dashed line is at $v_\phi = 150$ km s^{-1}, which is used to select disklike stars on highly prograde orbits. Note that the bins on v_ϕ used for the stars with [Fe/H] $\leqslant -3$ are twice the size for the more metal-rich stars, due to their lower numbers.

distribution of the arctangent of the $Z_{\rm max}/R_{\rm max}$ values (defined here as the IA) for VMP/EMP stars, following Haywood et al. (2018) and Di Matteo et al. (2020). The panels show this distribution for stars with the total numbers of VMP/EMP stars (black line), for stars with prograde orbits (purple line), and for stars with retrograde orbits (orange line), respectively, for stars in the regions with [Fe/H] $\leqslant -2$, -2.5, and -3. The vertical dashed line and dotted–dashed line show the approximate "troughs" in the distributions at IA $= 0.25$ and 0.65 rad, respectively, which can be used to roughly separate likely halo stars, thick-disk stars, and thin-disk stars. The numbers shown in each region listed in the figure reveal that VMP/EMP stars with prograde orbits dominate over those with retrograde orbits for IA $\leqslant 0.25$ rad and those with 0.25 rad $<$ IA $\leqslant 0.65$ rad, and much less so for IA > 0.65 rad. One can reasonably associate the prograde stars with IA $\leqslant 0.25$ rad with thin-disk orbits, those with 0.25 rad $<$ IA $\leqslant 0.65$ rad with thick-disk orbits, and those with IA > 0.65 rad with halo-like orbits.

If we now specialize to the highly prograde stars with orbital velocities $v_\phi > 150$ km s^{-1} (indicated by the blue shaded region in Figure 7), the relative dominance of the stars in the disklike system for VMP/EMP stars becomes even clearer.

Figure 8 is a plot of $Z_{\rm max}$ versus $R_{\rm max}$ for the stars with [Fe/H] $\leqslant -2$, -2.5, and -3, in the left, middle, and right panels, respectively. The top panels of this figure show plots of the $Z_{\rm max}$ distribution as a function of $R_{\rm max}$ for the full sample of prograde stars ($v_\phi > 0$ km s^{-1}). The dashed and dotted–dashed lines correspond to the troughs shown in Figure 7 at IA $= 0.25$ and 0.65 rad, respectively. The number of stars is provided in the legend at the top of each panel. The bottom panels apply to the stars on highly prograde orbits ($v_\phi > 150$ km s^{-1}).

Figure 9 shows histograms of the eccentricity distribution for stars with [Fe/H] $\leqslant -2$, -2.5, and -3, respectively. The colors represent the same cuts on IA as in Figure 7: halo-like orbits with IA > 0.65 rad are shown with black lines, thick-disk orbits with 0.25 rad $<$ IA $\leqslant 0.65$ rad are shown with red lines, and thin-disk orbits with IA $\leqslant 0.25$ rad are shown with blue lines. From inspection of the top row of panels, which includes stars on both retrograde and prograde orbits, the candidate VMP/EMP thin-disk-like stars are broadly distributed over all eccentricities, while the candidate VMP/EMP thick-disk-like stars exhibit similar patterns to halo-like stars in all three ranges of [Fe/H]. However, in the bottom row of panels, the $v_\phi > 150$ km s^{-1} cut increases the relative dominance of VMP/EMP stars on disklike orbits, including for stars with ecc $\leqslant 0.4$.

In summary, a total of 1496 candidate VMP/EMP stars with $v_\phi > 150$ km s^{-1} are identified. The total numbers of highly prograde disklike candidates selected by the $Z_{\rm max}$ and Haywood criteria are 876 and 1476, respectively. There are 856 stars selected by both methods.

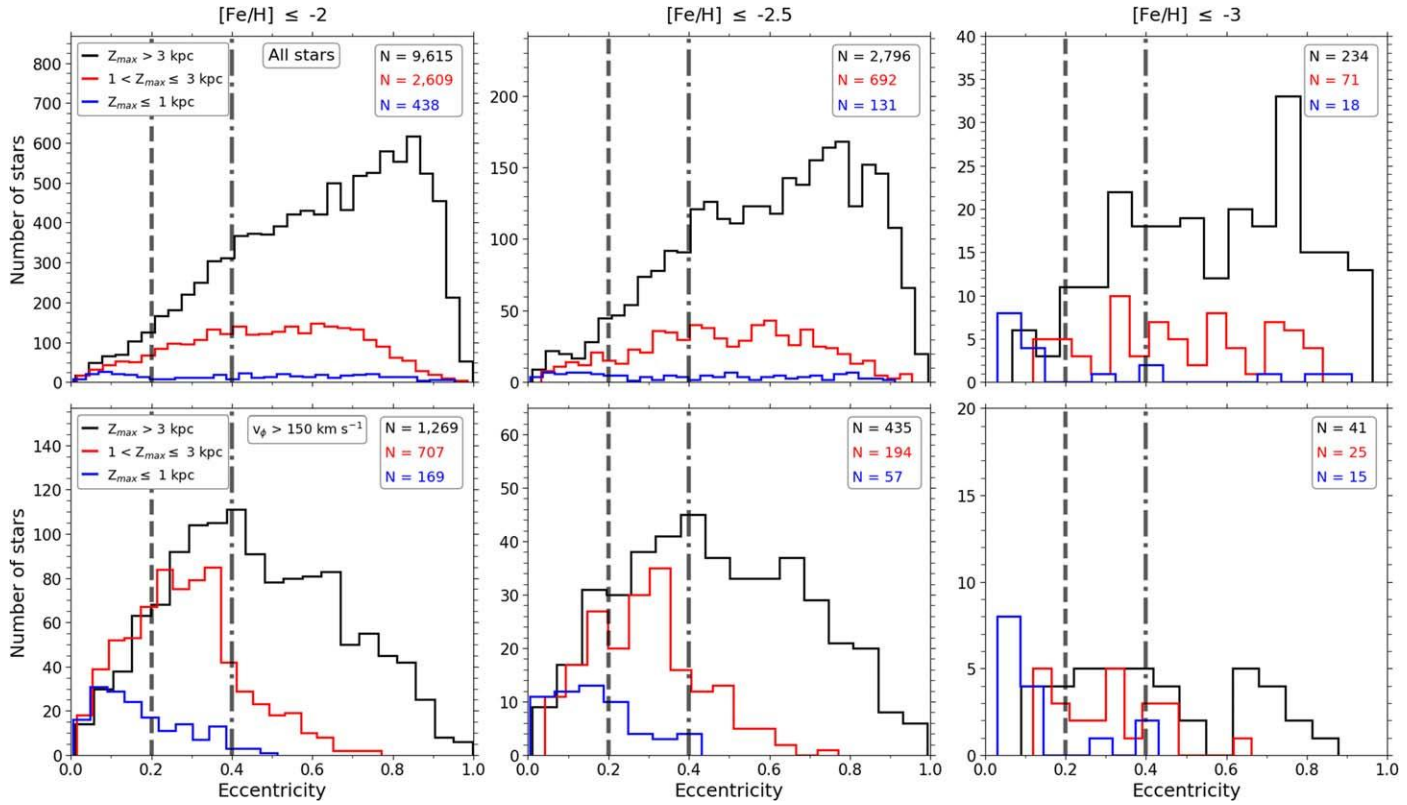

Figure 6. Top panels: number distributions of VMP/EMP stars on both retrograde and prograde orbits as a function of eccentricity, from the left to right panels, for [Fe/H] $\leqslant -2$, -2.5, and -3, respectively. The black, red, and blue solid lines indicate the stars with $Z_{\rm max} > 3$ kpc, 1 kpc $< Z_{\rm max} \leqslant 3$ kpc, and $Z_{\rm max} \leqslant 1$ kpc, respectively. The number of stars in each region is indicated in the legend in the upper right corner of the panels. The dashed and dotted–dashed lines are shown at ecc = 0.2 and 0.4, respectively. Bottom panels: same as the top panels, but for the highly prograde stars with $v_\phi > 150$ km s^{-1}.

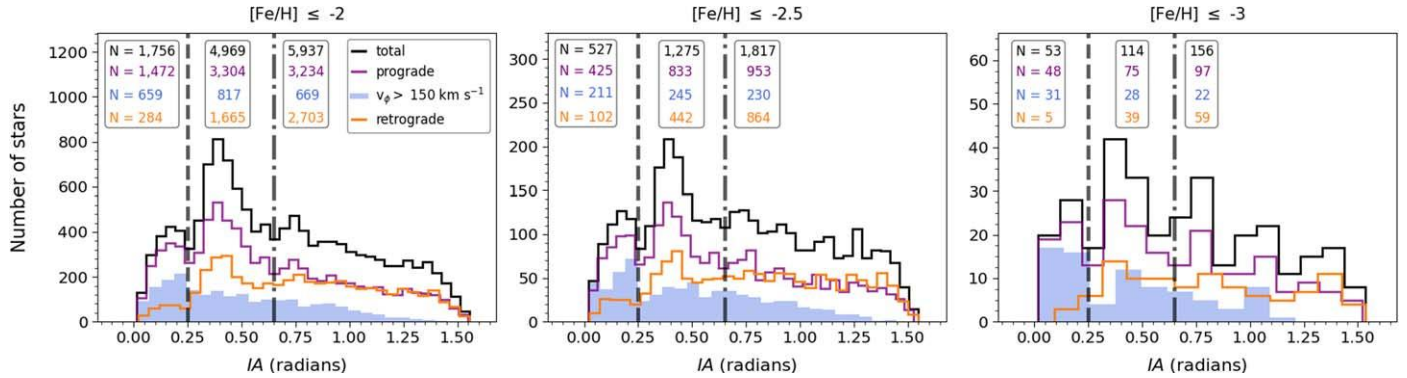

Figure 7. Number distribution of VMP/EMP stars as a function of IA, for [Fe/H] $\leqslant -2$, -2.5, and -3, from left to right, respectively. The total, prograde, and retrograde orbiting stars are shown with black, purple, and orange lines, respectively. The prograde stars with $v_\phi > 150$ km s^{-1} are shaded in blue. The number of stars in each region is indicated in the legend on the top of the panels. The dashed and dotted–dashed lines indicate IA = 0.25 and 0.65 rad, respectively.

4. Discussion

Separation based on the $Z_{\rm max}$ criterion, although capable of identifying a relatively pure sample of stars with halo-like orbits, has considerable potential contamination of stars with disklike orbits by halo-like stars. The Haywood criterion, based on the separation of stars in different dynamical populations, produces a purer sample of disklike stars, especially when the dominance of stars with thick- and thin-disk-like orbits over stars with halo-like orbits at ecc < 0.4 is considered in conjunction.

As we have demonstrated in this paper, the large numbers of stars now available with photometric-metallicity estimates from SMSS and SAGES have increased the numbers of candidate disk system VMP/EMP stars dramatically.

We refer to these stars as candidates for two reasons. First, although the photometric-metallicity estimates have a precision of $\sim$0.1 dex for [Fe/H] $\geqslant -1$ and approximately 0.3 dex at [Fe/H] ~ -3.5 to -4.0, comparable to those obtained from low to medium resolution ($R = \lambda/\Delta\lambda \sim 1800$) with a signal-to-noise ratio greater than 20 (Yanny et al. 2009; Luo et al. 2015; Rockosi et al. 2022), they may be influenced by the presence of strong molecular carbon bands, in particular for the most MP stars. We have taken steps to mitigate this behavior, as described in the Appendix, but they should be confirmed by follow-up spectroscopy. Second, the question remains whether at least some of the apparent disk system VMP/EMP stars represent members of an early-forming in situ primordial disk system, prior to additional stars being added from accreted

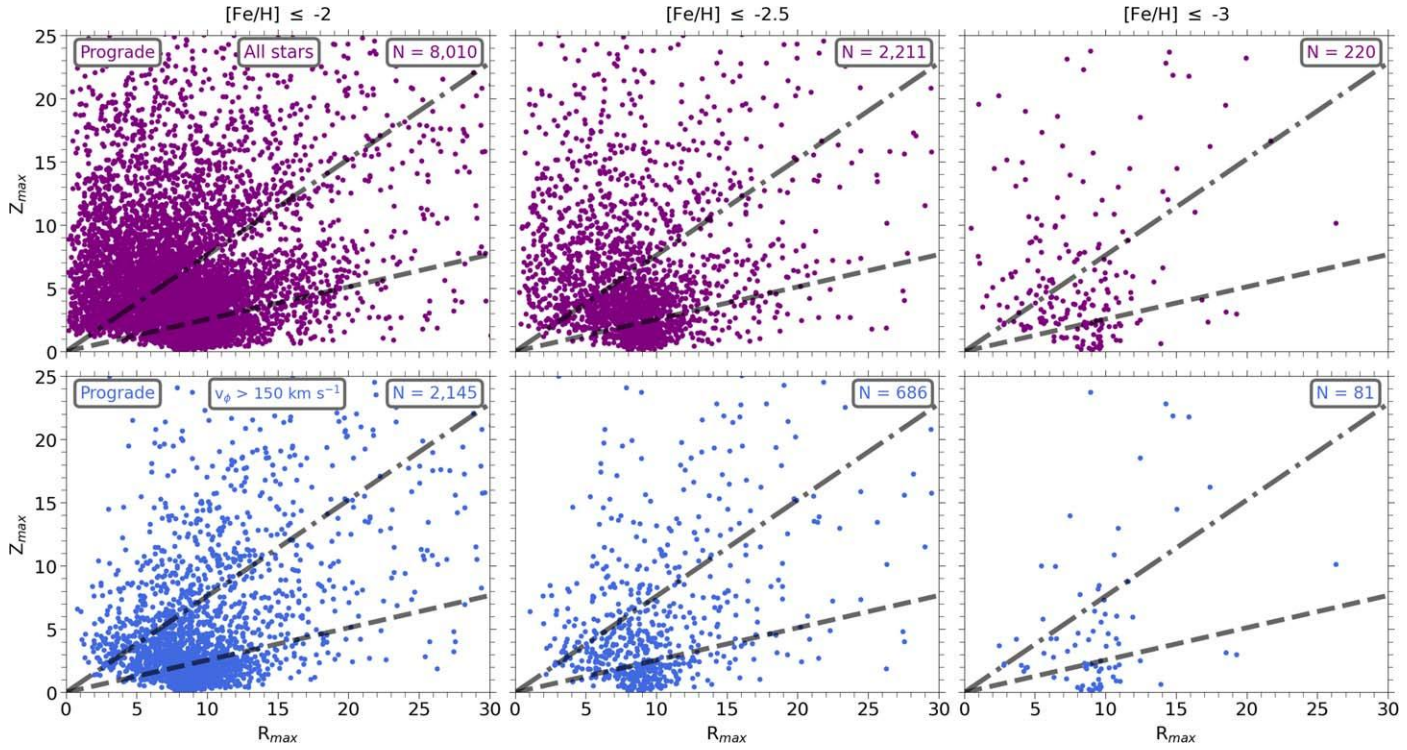

Figure 8. Top panels: the $Z_{\rm max}$ distribution as a function of $R_{\rm max}$ for the full sample of prograde stars. Dashed and dotted–dashed lines represent IA = 0.25 and 0.65 rad, respectively. The number of stars is shown in the legend at the top right of each panel. Bottom panels: same as the top panels, but for the stars with $v_\phi > 150$ km s^{-1}.

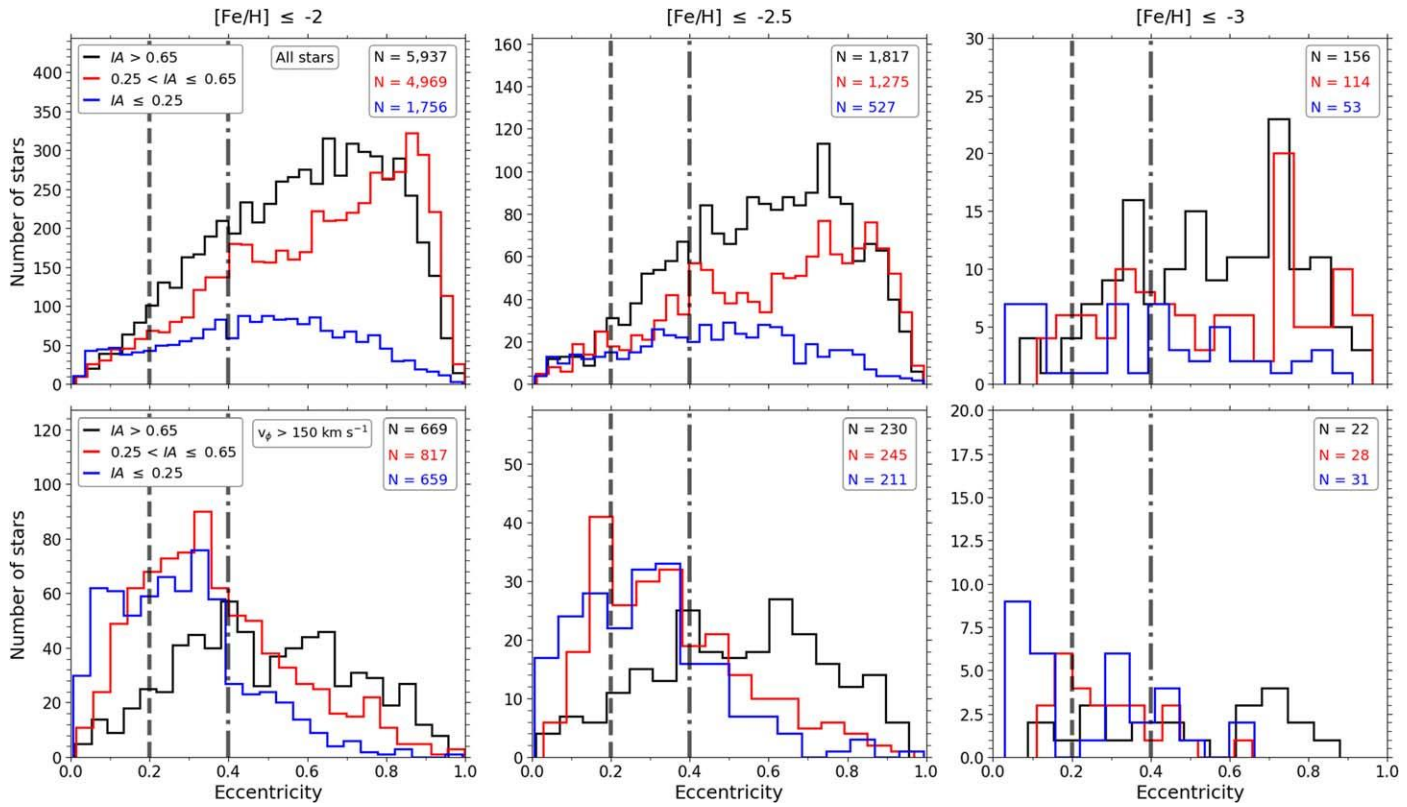

Figure 9. Top panels: number distributions of VMP/EMP stars as a function of eccentricity, from left to right, for [Fe/H] $\leqslant$2, 2.5, and 3, respectively. The black, red, and blue solid lines indicate the stars with IA $>$ 0.65 rad, 0.25 rad $<$ IA $\leqslant$ 0.65 rad, and IA $\leqslant$ 0.25 rad, respectively. The dashed and dotted–dashed lines are shown at ecc = 0.2 and 0.4, respectively. The number of stars in each region is indicated in the legend in the upper right corner of the panels. Bottom panels: same as in the top panels, but for the highly prograde stars with $v_\phi > 150$ km s^{-1}.

dwarf satellites, or are possibly a very/extremely low metallicity tail of the long-recognized MWTD component of the MW. These alternatives may prove difficult to differentiate between based on kinematics alone, as mergers with dwarf galaxies could readily perturb the orbits of stars that were born in a primordial thin or thick disk.

The best way to distinguish between these two possibilities may be to conduct a thorough study of their elemental abundances and look for differences as a function of declining metallicity. Feltzing & Feuillet (2023) have recently used elemental abundance information from APOGEE, in combination with kinematics, in order to identify the likely presence of an early disk structure in the inner disk of the MW including VMP stars (although they are limited by the lack of lower-metallicity stars in APOGEE, precluding verification that EMP stars are present as well). Detailed chemical abundances for our candidate VMP/EMP stars would clearly be useful.

Additional information should soon be available from the J-PLUS and S-PLUS photometric surveys, which can obtain estimates for C and Mg (as well as N and Ca, once ongoing calibrations are completed), in addition to [Fe/H], thanks to their narrow/medium-bandpass filters. More complete information will require high-resolution spectroscopic follow-up for at least a subset of the VMP/EMP candidates. Determination of more accurate age estimates than we have at present for candidate VMP/EMP stars on disklike orbits may also prove illuminating.

4.1. Comparison with Simulations

Beyond the identification of the VMP/EMP disk system candidates, we can speculate on their origins by considering numerical simulations of MW-like galaxies. We analyzed the data from a high-resolution cosmological zoom-in simulation of an MW-like galaxy with a halo mass of $1.2 \times 10^{12} M_{\odot}$ presented in Hirai et al. (2022). These authors defined the in situ component as stars formed in the main halo of the central galaxy, whereas the accreted component was defined as stars coming from dwarf galaxy satellites. Data within the Galactocentric distance $r_{\rm GC}$ between 3 and 20 kpc were considered; this region roughly corresponds to the observed region by SMSS and SAGES.

From this simulation, we found that 8% and 92% of stars with $v_{\phi} > 150$ km s^{-1} and [Fe/H] $\leqslant -2$ are formed in the in situ and accreted components, respectively. We also found that 96% of VMP/EMP stars with $v_{\phi} > 150$ km s^{-1} have ages >10 Gyr.

Similar results have been shown in the analysis of `IllustrisTNG50` simulations by Mardini et al. (2022a) and Carollo et al. (2023). Most recently, Sotillo-Ramos et al. (2023) considered a large sample of 138 MW analogs from the TNG50 cosmological simulations and found that, across all of these analogs, about 20% of the VMP/EMP stars have disklike orbits, with some analogs reaching as high as 30%. Roughly half of their disklike stars have average ages exceeding 12.5 Gyr, with 70% coming from accreted dwarf galaxies. Taken as a whole, the simulation results suggest that VMP/EMP stars with disklike orbits comprise stars coming primarily from accreted dwarf galaxies and in situ stars formed in an early primordial disk, or are associated with the MWTD.

Fractions of stars with prograde orbits can also inform the origin of VMP/EMP stars. Figure 10 compares the prograde fractions as a function of [Fe/H] for the combined SMSS/SAGES sample and the simulation results of Hirai et al. (2022).

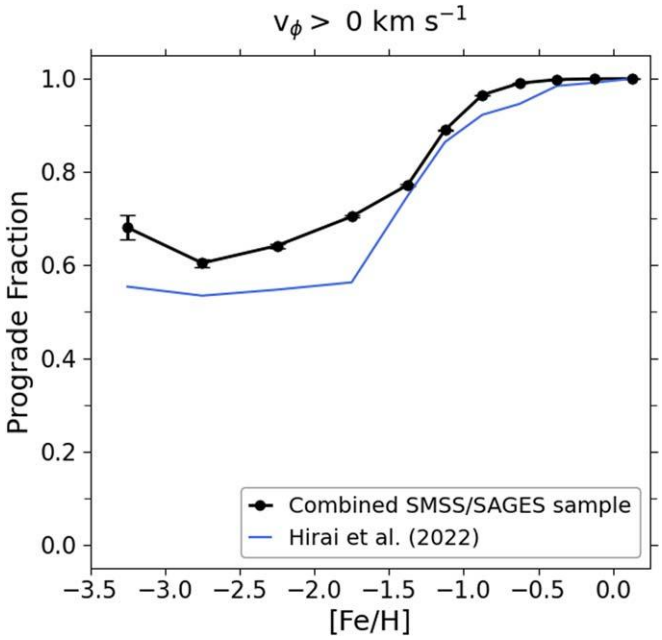

Figure 10. Fraction of prograde stars as a function of [Fe/H]. The black line shows the combined SMSS/SAGES sample. The blue line shows the simulation results of Hirai et al. (2022). The Galactocentric distance of the data considered is confined to between 3 and 20 kpc, roughly corresponding to the combined SMSS/SAGES sample. The error bars shown are calculated using the normal approximation for the binomial proportions; they are quite small owing to the large number of stars in our data set.

For [Fe/H] > -2.0, both our SMSS/SAGES sample and the simulation show an increasing trend toward higher metallicity, attributable to disk formation. On the other hand, the prograde fraction in our sample is roughly constant as a function of [Fe/H] for VMP/EMP stars. In the lowest-metallicity regime, the fraction rises to 0.68, reflecting the higher fraction of disklike orbits among EMP stars (Figures 6 and 9). This tendency is not clearly seen in the simulation. However, note that our sample's prograde fraction for VMP/EMP stars is significantly larger than that of the simulation. It should be kept in mind that the Hirai et al. (2022) simulation is for a single realization, when in fact a variety of galaxy assembly histories are likely to have different outcomes, as demonstrated by other recent simulation studies (e.g., Santistevan et al. 2021).

Prograde orbit fractions higher than 0.5 for [Fe/H] < -2 suggest the accretion of satellites preferentially on prograde orbits or early disk formation at low metallicity. Carter et al. (2021) also reported a high prograde fraction, between 0.7 and 0.8, but with significantly larger error bars owing to the smaller sample they considered (see the top left panel of their Figure 3). They have also shown that the prograde fraction converges to 0.5 with a model assuming an isotropic distribution of orbits in the stellar halo (Rybizki et al. 2018). We confirm their results with a larger sample. Recently, Li et al. (2022b) have shown that 10 out of 12 MW stellar streams with an average [Fe/H] ≈ -2 are on prograde orbits. These enhanced prograde fractions mean that the MW's VMP/EMP stars tend to be formed in accreted components with prograde orbits or in an ancient disk. As discussed above, spectroscopic follow-up of our candidate disklike VMP/EMP stars may help improve estimates of the relative fractions associated with these differing origins.

For convenience of future comparisons of our observations with those of others and with numerical simulations, Table 1

Table 1
Numbers, Fractions, and Orbital Characteristics of MP/VMP/EMP Stars in the SMSS/SAGES Sample

Full Sample of MP Stars				
	[Fe/H] $\leqslant -1$	[Fe/H] $\leqslant -2$	[Fe/H] $\leqslant -2.5$	[Fe/H] $\leqslant -3$
All ($N_{\rm tot} = 171{,}005$)	**171,005 (100.0%)**	**12,662 (7.4%)**	**3619 (2.1%)**	**323 (0.2%)**
Prograde	136,364 (79.7%)	8010 (63.3%)	2211 (61.1%)	220 (68.1%)
Retrograde	34,641 (20.3%)	4652 (36.7%)	1408 (38.9%)	103 (31.9%)
Dwarf	50,082 (29.3%)	2806 (22.2%)	804 (22.2%)	71 (22.0%)
Giant	120,923 (70.7%)	9856 (77.8%)	2815 (77.8%)	252 (78.0%)
	$-1 \geqslant$ [Fe/H] > -2	$-2 \geqslant$ [Fe/H] > -2.5	$-2.5 \geqslant$ [Fe/H] > -3	[Fe/H] $\leqslant -3$
All ($N_{\rm tot} = 171{,}005$)	**158,343 (92.6%)**	**9043 (5.3%)**	**3296 (1.9%)**	**323 (0.2%)**
Prograde	128,354 (81.1%)	5799 (64.1%)	1991 (60.4%)	220 (68.1%)
Retrograde	29,989 (18.9%)	3244 (35.9%)	1305 (39.6%)	103 (31.9%)
Dwarf	47,276 (29.9%)	2002 (22.1%)	733 (22.2%)	71 (22.0%)
Giant	111,067 (70.1%)	7041 (77.9%)	2563 (77.8%)	252 (78.0%)
$Z_{\rm max}$ Criterion Separation of Orbits for VMP/EMP Stars				
[Fe/H] $\leqslant -2$	$Z_{\rm max} > 3$ kpc	$Z_{\rm max} \leqslant 3$ kpc	1 kpc $< Z_{\rm max} \leqslant 3$ kpc	$Z_{\rm max} \leqslant 1$ kpc
All ($N_{\rm tot} = 12{,}662$)	**9615 (75.9%)**	**3047 (24.1%)**	**2609 (20.6%)**	**438 (3.5%)**
Prograde	5630 (58.6%)	2380 (78.1%)	2015 (77.2%)	365 (83.3%)
Retrograde	3985 (41.4%)	667 (21.9%)	594 (22.8%)	73 (16.7%)
Highly prograde	1269 (13.2%)	876 (28.7%)	707 (27.1%)	169 (38.6%)
Highly prograde, ecc $\leqslant 0.4$	552 (5.7%)	745 (24.5%)	582 (22.3%)	163 (37.2%)
Highly prograde, ecc $\leqslant 0.2$	147 (4.8%)	316 (10.4%)	205 (7.9%)	111 (25.3%)
[Fe/H] $\leqslant -2.5$	$Z_{\rm max} > 3$ kpc	$Z_{\rm max} \leqslant 3$ kpc	1 kpc $< Z_{\rm max} \leqslant 3$ kpc	$Z_{\rm max} \leqslant 1$ kpc
All ($N_{\rm tot} = 3619$)	**2796 (77.3%)**	**823 (22.7%)**	**692 (19.1%)**	**131 (3.6%)**
Prograde	1574 (56.3%)	637 (77.4%)	532 (76.9%)	105 (80.2%)
Retrograde	1222 (43.7%)	186 (22.6%)	160 (23.1%)	26 (19.8%)
Highly prograde	435 (15.6%)	251 (30.5%)	194 (28.0%)	57 (43.5%)
Highly prograde, ecc $\leqslant 0.4$	182 (6.5%)	209 (25.4%)	154 (22.3%)	55 (42.0%)
Highly prograde, ecc $\leqslant 0.2$	59 (2.1%)	94 (11.4%)	56 (8.1%)	38 (29.0%)
[Fe/H] $\leqslant -3$	$Z_{\rm max} > 3$ kpc	$Z_{\rm max} \leqslant 3$ kpc	1 kpc $< Z_{\rm max} \leqslant 3$ kpc	$Z_{\rm max} \leqslant 1$ kpc
All ($N_{\rm tot} = 323$)	**234 (72.4%)**	**89 (27.6%)**	**71 (22.0%)**	**18 (5.6%)**
Prograde	144 (61.5%)	76 (85.4%)	58 (81.7%)	18 (100.0%)
Retrograde	90 (38.5%)	13 (14.6%)	13 (18.3%)	0 (0.0%)
Highly prograde	41 (17.5%)	40 (44.9%)	25 (35.2%)	15 (83.3%)
Highly prograde, ecc $\leqslant 0.4$	21 (9.0%)	31 (34.8%)	18 (25.4%)	13 (72.2%)
Highly prograde, ecc $\leqslant 0.2$	7 (3.0%)	19 (21.3%)	7 (9.9%)	12 (66.7%)
Haywood Criterion Separation of Orbits for VMP/EMP Stars				
[Fe/H] $\leqslant -2$	IA > 0.65	IA $\leqslant 0.65$	$0.25 <$ IA $\leqslant 0.65$	IA $\leqslant 0.25$
All ($N_{\rm tot} = 12{,}662$)	**5937 (46.9%)**	**6725 (53.1%)**	**4969 (39.2%)**	**1756 (13.9%)**
Prograde	3234 (54.5%)	4776 (71.0%)	3304 (66.5%)	1472 (83.8%)
Retrograde	2703 (45.5%)	1949 (29.0%)	1665 (33.5%)	284 (16.2%)
Highly prograde	669 (11.3%)	1476 (21.9%)	817 (16.4%)	659 (37.5%)
Highly prograde, ecc $\leqslant 0.4$	249 (4.2%)	1048 (15.6%)	734 (14.8%)	532 (30.3%)
Highly prograde, ecc $\leqslant 0.2$	59 (1.0%)	404 (6.0%)	186 (3.7%)	237 (13.5%)
[Fe/H] $\leqslant -2.5$	IA > 0.65	IA $\leqslant 0.65$	$0.25 <$ IA $\leqslant 0.65$	IA $\leqslant 0.25$
All($N_{\rm tot} = 3619$)	**1817 (50.2%)**	**1802 (49.8%)**	**1275 (35.2%)**	**527 (14.6%)**
Prograde	953 (52.4%)	1258 (69.8%)	833 (65.3%)	425 (80.6%)
Retrograde	864 (47.6%)	544 (30.2%)	442 (34.7%)	102 (19.4%)
Highly prograde	230 (12.7%)	456 (25.3%)	245 (19.2%)	211 (40.0%)
Highly prograde, ecc $\leqslant 0.4$	69 (3.8%)	322 (17.9%)	211 (16.5%)	163 (30.9%)
Highly prograde, ecc $\leqslant 0.2$	18 (1.0%)	135 (7.5%)	67 (5.3%)	72 (13.7%)
[Fe/H] $\leqslant -3$	IA > 0.65	IA $\leqslant 0.65$	$0.25 <$ IA $\leqslant 0.65$	IA $\leqslant 0.25$
All ($N_{\rm tot} = 323$)	**156 (48.3%)**	**167 (51.7%)**	**114 (35.3%)**	**53 (16.4%)**
Prograde	97 (62.2%)	123 (73.7%)	75 (65.8%)	48 (90.6%)
Retrograde	59 (37.8%)	44 (26.3%)	39 (34.2%)	5 (9.4%)
Highly prograde	22 (14.1%)	59 (35.3%)	28 (24.6%)	31 (58.5%)
Highly prograde, ecc $\leqslant 0.4$	8 (5.1%)	44 (26.3%)	29 (25.4%)	22 (41.5%)
Highly prograde, ecc $\leqslant 0.2$	2 (1.3%)	24 (14.4%)	9 (7.9%)	15 (28.3%)

provides a summary of the numbers, fractions, and orbital characteristics of the SMSS/SAGES sample for different cuts on [Fe/H], $Z_{\rm max}$, and IA. Note that, except for the first line in each subsection of the table (indicated as "All"), the fractions refer to the total numbers of stars listed on the first line at the top of each column in the subsection (shown in bold).

5. Summary

We have identified 1496 candidate VMP/EMP disk system stars in the MW from a subset of the ∼50 million stars from SMSS and SAGES with available photometric-metallicity estimates, based on calibrated $u - G_{BP}$ colors and $v - G_{BP}$ colors, a combination of the u/v bands from SMSS/SAGES, and the ultra-wide-band Gaia G_{BP} prism spectra (Huang et al. 2022, 2023). We then trimmed the combined sample, eliminating photometrically identified binaries, cool dwarfs, and likely members of globular clusters. We then obtain the subset of 7.19 million stars in the combined sample with available RVs, proper motions, and distance estimates.

After the determination of dynamical parameters, we remove likely unbound stars and excise stars with errors in their orbital rotation velocities $v_\phi > 25$ km s^{-1} and relative errors in Z_{max} (maximum orbital distance from the Galactic plane) and in R_{max} (maximum orbital apocentric distance projected on to the plane) >30%, leaving a total sample of about 5.86 million stars.

We then apply two methods to separate stars with halo-like and disklike orbits. The first approach considered stars with $Z_{max} > 3$ kpc to have halo-like orbits and those with $Z_{max} \leqslant 3$ kpc to have disklike orbits. Our analysis indicates that there exists a significant population of candidate VMP/EMP disk system stars, moving on rapid prograde orbits ($v_\phi > 150$ km s^{-1}), increasing their relative populations with declining metallicity. We also split the stars with disklike orbits into the regions 1 kpc $< Z_{max} \leqslant 3$ kpc and $Z_{max} \leqslant 1$ kpc, in an attempt to better isolate stars with thick-disk orbits from those with thin-disk orbits. Based on this criterion, we find that 28.7% of the VMP stars with $Z_{max} \leqslant 3$ kpc have highly prograde disklike orbits (707 stars on thick-disk orbits, 169 stars on thin-disk orbits), while 44.9% of the EMP stars have highly prograde disklike orbits (25 on thick-disk orbits, 15 on thin-disk orbits). These fractions increase further if one also takes the eccentricity of the orbits into account.

The second approach considered the stars populating wedges in the diagram of Z_{max} versus IA, which redistributes corresponding to different dynamical populations of stars with halo-like and disklike orbits. Our analysis indicates that there exists a significant population of candidate VMP/EMP disk system stars moving on rapid prograde orbits ($v_\phi > 150$ km s^{-1}), increasing their relative populations with declining metallicity. Based on the Haywood criterion, we find that 21.9% of the VMP stars have highly prograde disklike orbits (817 stars on thick-disk orbits, 659 stars on thin-disk orbits), while 35.3% of the EMP stars have highly prograde disklike orbits (28 stars on thick-disk orbits, 31 stars on thin-disk orbits). These fractions increase further if one also takes the eccentricity of the orbits into account.

In the near future, the astrophysical properties and origin of these stars will be examined further with data from the large-scale Javalambre/Southern Photometric Local Universe Surveys (J/S-PLUS). These surveys include additional narrow/medium-band filters that allow for photometric estimates of C, N, Mg, and Ca abundances, once ongoing calibration efforts are completed. Of importance, it will then be possible to greatly reduce the influence of carbon on the metallicity estimates, which affect our current SMSS/SAGES sample, as [C/Fe] can be estimated separately from the [Fe/H]. The accuracy and precision of the derived metallicities will be improved as well.

In order to confirm the metallicities and elemental abundance estimates (such as the α-elements or carbonicity, [C/Fe]) for the VMP/EMP stars with disklike orbits, we require medium-resolution spectroscopic follow-up for the catalog of ∼1500 VMP/EMP stars in our sample. High-resolution spectroscopic follow-up of at least the most interesting subset of these would also be useful. The full catalog of VMP/EMP stars with disklike orbits is listed in the Appendix and will be made available online. Determinations of age estimates for our candidate VMP/EMP stars would also help to place constraints on their origins. Nevertheless, our present finding that large fractions of VMP/EMP stars are kinematically associated with the rapidly rotating MW disk system (in particular those at low eccentricity) strongly suggests the presence of an early-forming "primordial" disk.

Acknowledgments

The authors express thanks to Deokkeun An for his thoughts and comments on an early version of this paper. We are also grateful to Evan Kirby and Borja Anguiano for their input as well. The authors thank an anonymous referee for their helpful comments that greatly improved this paper.

The Stellar Abundance and Galactic Evolution Survey (SAGES) is a multiband photometric project built and managed by the Research Group of the Stellar Abundance and Galactic Evolution of the National Astronomical Observatories, Chinese Academy of Sciences (NAOC).

This work was supported in part by grant PHY 14-30152, Physics Frontier Center/JINA Center for the Evolution of the Elements (JINA-CEE), and by OISE-1927130: The International Research Network for Nuclear Astrophysics (IReNA), awarded by the US National Science Foundation. Y.S.L. acknowledges support from the National Research Foundation (NRF) of Korea grants funded by the Ministry of Science and ICT (NRF-2021R1A2C1008679 and RS-2024-00333766). Y. S.L. also gratefully acknowledges partial support for his visit to the University of Notre Dame from OISE-1927130: The International Research Network for Nuclear Astrophysics (IReNA), awarded by the US National Science Foundation. Y. Huang acknowledges support from the National Key R&D Program of China No. 2019YFA0405500 and National Natural Science Foundation of China grants 11903027 and 11833006. Y. Hirai was supported by JSPS KAKENHI grant Nos. JP22KJ0157, JP21H04499, JP21K03614, and JP22H01259. Numerical computations were in part carried out on Cray XC50 and computers at the Center for Computational Astrophysics, National Astronomical Observatory of Japan. S.X. acknowledges support from the National Natural Science Foundation of China through project NSFC 12222301. K.T. was supported by the National Natural Science Foundation of China under grant Nos. 12261141689, 12090044, and 12090040. G.Z. acknowledges support by the National Natural Science Foundation of China under grant Nos. 11988101 and 11890694.

Appendix

Table A1 provides a description of the parameters we report for candidate VMP/EMP stars from the combined SMSS/SAGES sample, based on the information provided by Huang et al. (2022, 2023). We included stars with adopted photometric-metallicity estimates in the range $-4.0 <$ [Fe/H] $\leqslant -2.0$, based on the individual u-band and v-band filters, as well as their combination. Note that, for completeness, we have included information for all of the stars with available photometric-metallicity estimates, regardless of their

Table A1
Description of the Candidate VMP/EMP Stars in the Combined SMSS/SAGES Sample

Field	Description[a]	Unit
Gaia DR3	The Gaia DR3 Source ID [source_id]	…
R.A.	The R.A. from SMSS DR2 and SAGES DR1 (J2000)	hours : minutes : seconds
Decl.	The decl. from SMSS DR2 and SAGES DR1 (J2000)	degrees : minutes : seconds
GCmag	The calibration-corrected G magnitude by Huang et al. (2022, 2023) for the Gaia DR3 [G_C]	…
e_GCmag	The calibration-corrected G magnitude uncertainty by Huang et al. (2022, 2023) for the Gaia DR3 [err_G_C]	…
BR0	The intrinsic colors of $(G_{BP}\ G_{RP})_0$ by Huang et al. (2022, 2023) [br0]	…
e_BR0	The intrinsic colors uncertainty of $(G_{BP}\ G_{RP})_0$ by Huang et al. (2022, 2023) [err_br0]	…
E(B–V)	The $E(B–V)$ from the extinction map of Schlegel et al. (1998), corrected by Huang et al. (2022, 2023) [ebv_sfd]	…
FeH-UB/VB/UVB	The photometric-metallicity estimates from Huang et al. (2022, 2023) [feh]. The "ub," "vb," and "uvb" indicate the stellar color(s) used in estimating [Fe/H] by Huang et al. (2022, 2023)	…
e_FeH-UB/VB/UVB	The photometric-metallicity estimates uncertainty from Huang et al. (2022, 2023) [err_feh]	dex
Teff	The effective temperature from Huang et al. (2022, 2023) [Teff]	K
e_Teff	The effective temperature uncertainty from Huang et al. (2022, 2023) [err_Teff]	K
Dist	The distance from Huang et al. (2022, 2023) [dist_adop]	kpc
e_Dist	The distance uncertainty from Huang et al. (2022, 2023) [err_dist_adop]	kpc
f_Dist	Flag with "parallax" if the distance is derived by parallax, "CAF," "CMD_dwarf," "CMD_dwarf_nobia," and "CMD_giant" if the distance is derived by color–absolute magnitude fiducial relations from Huang et al. (2022, 2023) [dist_adop_flg]	…
RVel	The RV from Huang et al. (2022, 2023) [rv_adop]	km s^{-1}
e_RVel	The RV uncertainty from Huang et al. (2022, 2023) [err_rv_adop]	km s^{-1}
f_RVel	Flag with "Gaia DR3," "GALAH," "LM-DR9," "APG-DR17," "AEGIS," "SEGUE," "Gaia," "Gaia-ESO," "LAMOST," "RAVE," "LIT," and "BB" to indicate the source of RV from Huang et al. (2022), and "Gaia DR3," "LAMOST," "SEGUE," "APOGEE," "GALAH," and "RAVE" from Huang et al. (2023) [rv_adop_flg]	…
plx	The parallax from Gaia DR3 [parallax]	mas
e_plx	The parallax uncertainty from Gaia DR3 [parallax_error]	mas
pmRA	The proper motion in the R.A. from Gaia DR3 [pmra]	mas yr^{-1}
e_pmRA	The proper motion uncertainty in the R.A. from Gaia DR3 [pmra_error]	mas yr^{-1}
pmDE	The proper motion in the decl. from Gaia DR3 [pmdec]	mas yr^{-1}
e_pmDE	The proper-motion uncertainty in the decl. from Gaia DR3 [pmdec_error]	mas yr^{-1}
pmRApmDEcor	The correlation coefficient between the proper motion in R.A. and in decl. from Gaia DR3	…
Type	Flag with "Dwarf" and "Giant" from Huang et al. (2022, 2023)	…
SubType	Flag with "TO" for turn-off stars and "MS" for main-sequence stars from Huang et al. (2022, 2023)	…
vPHI	The rotational velocity as given by AGAMA	km s^{-1}
e_vPHI	The rotational velocity uncertainty as given by Monte Carlo sampling through AGAMA	km s^{-1}
E	The orbital energy as given by AGAMA	$km^2\ s^{-2}$
e_E	The orbital energy uncertainty as given by AGAMA	$km^2\ s^{-2}$
Jr,Jphi,Jz	The cylindrical actions as given by AGAMA	kpc km s^{-1}
e_Jr,e_Jphi,e_Jz	The cylindrical actions uncertainty as given by AGAMA	kpc km s^{-1}
rperi	The Galactic pericentric distance as given by AGAMA	kpc
e_rperi	The Galactic pericentric distance uncertainty as given by AGAMA	kpc
rapo	The Galactic apocentric distance as given by AGAMA	kpc
e_rapo	The Galactic apocentric distance uncertainty as given by Monte Carlo sampling through AGAMA	kpc
Zmax	The maximum height above the Galactic plane as given by AGAMA	kpc
e_Zmax	The maximum height uncertainty above the Galactic plane as given by Monte Carlo sampling through AGAMA	kpc
relerr-Zmax	The relative uncertainty of the maximum height above the Galactic plane	…
Rmax	The projection of the Galactic apocentric distance onto the Galactic plane as given by $\sqrt{r_{apo}^2 - Z_{max}^2}$	kpc
relerr-Rmax	The relative uncertainty of the projection of the Galactic apocentric distance onto the Galactic plane. The uncertainty is as given by Monte Carlo sampling through AGAMA	…
IA	The inclination angle defined as the arctangent ratio of (Z_{max}/R_{max})	rad
ecc	The eccentricity as given by $(r_{apo} - r_{peri})/(r_{apo} + r_{peri})$ through AGAMA	…
criterion	Flag with "Z_{max}," "Haywood," or "Both" to indicate the criterion used for the separation of stars on halo-like orbits from those on thick-disk-like orbits and thin-disk-like orbits	…

Note.
[a] The original column labels from Huang et al. (2022, 2023) or Gaia DR3 are given in square brackets in the column description.

(This table is available in its entirety in machine-readable form.)

metallicities obtained by any filters, errors in their derived metallicities, or reddening. The full table of 1,291,424 stars is made available online.

Table A2 is a listing of the candidate VMP/EMP stars on disklike orbits that we employ, providing the data needed for further analysis and/or spectroscopic follow-up observations.

Table A2
1496 VMP/EMP Disklike Candidate Stars in the Combined SMSS/SAGES Sample

Source ID	R.A. (J2000)	Decl. (J2000)	G_C	$G_{BP} - G_{RP}$	Type	Dist (kpc)	[Fe/H]	$\mathrm{err}_{[Fe/H]}$ (dex)	v_ϕ (km s^{-1})	Z_{max} (kpc)	R_{max} (kpc)	IA (rad)	ecc	Criterion
4918300611248859648	00:00:09.07	−59:03:26.0	14.67	0.89	G	2.48	−2.10	0.15	179.3	2.5	7.2	0.33	0.175	Both
2853059333495692800	00:00:18.21	+25:05:15.2	17.99	1.08	D	1.65	−2.01	0.33	160.3	1.3	8.9	0.14	0.317	Both
2853263288606167808	00:00:58.03	+26:00:23.4	17.98	0.99	D	2.76	−2.21	0.33	170.5	2.1	9.4	0.22	0.271	Both
2880219431068389632	00:02:39.84	+36:50:18.5	17.73	0.87	D	2.14	−2.06	0.35	224.8	1.1	10.1	0.11	0.125	Both
2421349012110147840	00:03:51.14	−12:31:54.1	12.65	1.03	G	2.77	−2.24	0.06	181.5	3.4	8.9	0.36	0.252	Haywood
2876918628442545152	00:06:55.97	+35:54:29.0	17.50	0.84	D	2.18	−2.70	0.21	190.7	1.0	9.1	0.10	0.171	Both
2546602108275485568	00:06:57.29	+01:15:53.4	17.26	0.72	D	1.83	−2.66	0.20	158.5	1.8	9.4	0.19	0.384	Both
2319766674712899840	00:07:42.57	−30:56:13.4	11.72	0.96	G	1.57	−2.08	0.04	179.0	2.0	8.2	0.23	0.240	Both
2739001632226213504	00:08:36.17	+02:34:11.1	17.26	0.70	D	1.86	−2.53	0.21	162.1	5.9	12.6	0.44	0.513	Haywood
2443519530213095168	00:09:47.75	−06:15:31.9	17.60	1.01	D	1.66	−2.16	0.14	174.9	1.9	8.4	0.23	0.238	Both
2546356509161321600	00:11:08.63	+00:59:50.1	15.42	0.73	D	1.06	−2.12	0.08	151.5	1.1	10.5	0.10	0.491	Both
2740672133986589568	00:12:26.18	+03:34:41.9	16.52	0.63	D	1.79	−2.21	0.19	160.3	2.0	8.9	0.22	0.333	Both
2850385316920406016	00:14:20.01	+25:45:11.1	17.15	1.05	D	1.17	−2.12	0.19	195.2	1.3	9.3	0.14	0.218	Both
395035668663587328	00:15:24.23	+51:39:07.5	13.23	0.68	D	0.78	−3.18	0.08	239.3	0.2	9.1	0.02	0.030	Both
2768462152939050112	00:17:21.85	+14:49:24.1	16.57	0.62	D	1.40	−2.10	0.21	167.2	1.2	10.0	0.12	0.387	Both
2428249340927211008	00:18:20.37	−09:18:32.9	15.43	0.64	D	1.24	−2.66	0.36	165.3	2.1	9.4	0.22	0.372	Both
2800378157994808576	00:18:48.76	+22:15:30.1	16.28	0.80	D	1.17	−2.37	0.12	195.0	4.6	18.1	0.25	0.609	Haywood
2876157251000218496	00:18:56.93	+34:54:44.3	17.12	0.79	D	2.03	−2.84	0.27	231.4	1.0	10.3	0.10	0.111	Both
4991862612070916736	00:22:18.35	−43:31:15.4	14.36	0.82	G	2.13	−2.68	0.30	185.0	4.3	8.2	0.49	0.197	Haywood
2864157352892856576	00:22:27.17	+34:34:14.0	18.43	0.85	D	3.30	−2.68	0.35	155.2	2.8	12.6	0.22	0.491	Both
378314738205895296	00:23:19.23	+36:02:21.5	17.73	0.86	D	2.29	−2.12	0.30	188.3	4.2	9.5	0.41	0.165	Haywood
2747658873250089600	00:23:27.30	+06:25:53.5	17.40	0.87	D	1.63	−2.23	0.20	210.7	16.6	25.0	0.58	0.692	Haywood
2855523884512993792	00:24:08.92	+26:09:43.0	17.67	0.74	D	2.53	−2.06	0.33	220.7	1.6	9.4	0.17	0.055	Both
2367276232846933760	00:26:35.09	−17:49:21.4	16.62	0.62	D	2.67	−2.28	0.39	231.7	6.5	10.7	0.55	0.195	Haywood
2800046311641547392	00:26:49.64	+22:30:39.2	14.57	0.95	G	5.83	−2.62	0.09	185.4	6.4	10.9	0.53	0.161	Haywood
2426849250308221696	00:28:21.09	−08:46:37.8	13.48	0.98	G	3.77	−2.31	0.06	161.2	6.4	9.7	0.58	0.342	Haywood
4918673723647798528	00:30:35.34	−57:32:26.5	13.88	0.94	G	3.57	−2.22	0.12	180.5	3.2	7.6	0.40	0.215	Haywood
2806067477833582336	00:32:20.46	+23:14:27.8	13.24	0.67	D	0.42	−2.75	0.03	222.7	0.3	10.3	0.03	0.232	Both
2542770623787256576	00:34:51.59	−00:28:22.3	17.45	1.00	D	1.58	−2.20	0.20	250.2	2.0	11.3	0.18	0.181	Both
2750377553188528512	00:35:21.56	+09:37:58.8	17.54	0.69	D	2.10	−2.22	0.29	167.2	2.6	12.1	0.21	0.481	Both
2425850893750224000	00:38:34.18	−10:03:57.2	16.61	0.66	D	2.18	−2.68	0.44	296.2	4.6	17.0	0.26	0.359	Haywood
2781291215956696704	00:43:40.61	+15:30:11.6	17.54	0.88	D	1.68	−2.14	0.27	176.3	1.5	10.7	0.14	0.379	Both
2776361869106548992	00:45:00.93	+13:45:45.6	16.95	0.82	D	0.88	−2.28	0.17	238.8	10.2	14.3	0.62	0.359	Haywood
2530949495102121600	00:46:02.00	−00:26:48.1	16.65	0.72	D	1.74	−2.24	0.09	164.1	1.8	9.7	0.18	0.364	Both
2776181789717803008	00:48:25.66	+13:41:47.4	13.84	0.84	G	2.27	−2.50	0.40	191.3	2.5	12.7	0.19	0.409	Both
4999763977506992256	00:55:17.54	−38:28:37.7	14.23	0.64	D	0.94	−2.42	0.23	202.9	1.0	8.7	0.11	0.181	Both
378064947205609984	00:55:28.52	+46:24:06.5	13.77	1.09	G	0.86	−2.03	0.03	151.6	0.6	8.8	0.07	0.357	Both
364777486620366976	00:55:46.05	+38:18:03.6	17.28	0.64	D	1.96	−2.07	0.35	198.6	1.0	9.6	0.11	0.172	Both
2357297065313248512	00:57:51.87	−18:12:25.9	12.74	0.62	D	0.44	−2.54	0.15	185.3	0.9	8.7	0.10	0.239	Both
2553447805108682496	00:58:27.10	+06:33:56.4	12.25	1.08	G	3.51	−2.62	0.02	165.1	3.2	11.0	0.29	0.367	Haywood
374902167646414720	01:00:04.74	+43:02:08.5	15.11	1.19	G	18.53	−2.29	0.07	182.7	14.2	27.7	0.47	0.311	Haywood
4710497998840333568	01:01:03.19	−62:17:20.8	13.48	0.97	G	3.61	−2.50	0.07	234.9	8.8	16.5	0.49	0.537	Haywood
4684461048100616448	01:01:30.40	−75:44:51.0	14.04	1.01	G	7.28	−2.13	0.05	156.3	5.6	8.3	0.60	0.371	Haywood
2536647615329253376	01:02:09.79	+01:03:49.3	15.92	0.72	D	0.40	−2.34	0.09	172.9	0.5	8.6	0.06	0.279	Both
2788522394695432704	01:02:50.31	+19:26:45.8	17.58	0.65	D	2.09	−2.41	0.29	235.7	1.7	10.6	0.16	0.110	Both
2536576662469536768	01:03:30.39	+00:43:47.5	17.13	0.61	D	1.44	−2.70	0.29	187.7	1.3	8.6	0.15	0.181	Both
4926978266253100672	01:03:32.61	−53:46:54.4	13.98	0.95	G	4.17	−2.35	0.10	203.4	5.9	8.4	0.61	0.164	Haywood
2538090861779751424	01:04:23.30	+01:00:00.8	17.73	0.70	D	2.17	−2.73	0.24	155.9	2.6	9.4	0.27	0.346	Both
369849739917996544	01:07:30.66	+38:22:04.8	17.23	0.70	D	1.45	−3.14	0.35	224.5	0.7	9.1	0.07	0.044	Both

(This table is available in its entirety in machine-readable form.)

From the candidates of Table A1, we only included the stars with errors in their adopted metallicities $\mathrm{err}_{[\mathrm{Fe/H}]} \leqslant 0.5$ dex and stars with a difference of less than ± 0.5 dex between the u-band- and v-band-based abundances ($|[\mathrm{Fe/H}]_{ub} - [\mathrm{Fe/H}]_{vb}|$). For the reddening cut, the numbers of stars that would be excluded, depending on $E(B-V) \leqslant 0.1$, 0.2, 0.3, 0.4, and 0.5, are approximately 1.72 million, 0.23 million, 17,000, 2, and 0, respectively. The numbers of VMP/EMP stars that would be removed by these cuts are about 3000, 500, 5, and no VMP/EMP stars for $E(B-V) > 0.4$. Thus, we chose to only include the stars with $E(B-V) \leqslant 0.3$ for our analysis. We also included stars having derived errors in their orbital rotation velocities $v_\phi \leqslant 25$ km s^{-1} and relative errors in $Z_{\max} \leqslant 0.30$ and $R_{\max} \leqslant 0.30$.

Figure A1 compares our photometric-metallicity estimates (based on the $u - G_{\mathrm{BP}}$ colors, the $v - G_{\mathrm{BP}}$ colors, and, when available, the combination of these colors; see Huang et al. 2022, 2023) to medium- and high-resolution spectroscopic estimates with available [Fe/H] and [C/Fe] (not corrected for evolutionary effects) from a number of literature sources, including bright stars from Gaia DR3 with spectroscopic metallicity estimates obtained by Viswanathan et al. (2024), based on a refined analysis of the Radial Velocity Spectrometer spectra. The left column of panels shows the results from the full set of available stars in our catalog, while the right column of panels excludes the (recognized) carbon-enhanced metal-poor (CEMP; Beers & Christlieb 2005) stars that satisfy [C/Fe] $> +0.7$. The black solid line in each panel is a linear regression for the metallicity region, excluding stars with $[\mathrm{Fe/H}]_{\mathrm{Literature}} \leqslant 3.0$, indicated with the light-blue shaded region. The dashed lines represent the one-to-one lines. The legends in each panel indicate the number of matching stars (N), the p-value, and the r^2 value (which indicates the fraction of variance that can be accounted for by the regression relationship) found by the Pearson correlation analysis, as well as the biweight location (μ) and scale (σ) of the metallicity residuals (see Beers et al. 1990). The top, middle, and bottom panels apply to matching stars with available $[\mathrm{Fe/H}]_{ub}$, $[\mathrm{Fe/H}]_{vb}$, and $[\mathrm{Fe/H}]_{ub+vb}$, respectively.

From inspection of this figure, it is apparent that excluding (recognized) CEMP stars results in linear regression lines that are aligned more closely to the one-to-one relationships, particularly in the middle and bottom panels.[17] This trend is supported by the higher r^2 values and smaller biweight residual location offsets and scale values shown in the right column of panels. It is evident that stars with enhanced carbon result in higher derived photometric-metallicity estimates in our analysis. The largest deviations are found when considering the photometric-metallicity estimates based solely on the u band (top row of panels). Smaller deviations are found when considering the photometric-metallicity estimates based solely on the v band (middle row of panels). The combination of the u-band and v-band photometric-metallicity estimates, as seen from the bottom row of panels, somewhat mitigates the effects of carbon enhancement, resulting in acceptably small offsets and lower dispersions. However, it is clear that our photometric-metallicity estimates for stars with literature estimates of [Fe/H] are most likely to be higher when carbon is enhanced, in particular for EMP stars.

The above results motivate our choice to only include stars with photometric-metallicity estimates based on the stars for which acceptable estimates are obtained based either solely on the v band or on the combination of the u band and v band, but excluding stars that have estimates based solely on the u band. From this comparison, and under the assumption that the spectroscopic estimates of [Fe/H] from multiple sources themselves can account for a "sample-to-sample" scatter (arising from different assumptions made by the individual analyses) on the order of 0.15–0.20 dex, the external errors of the photometric-metallicity estimates range from 0.20 to 0.35 dex (and on the order of 0.10–0.15 dex for stars more metal-rich than considered here). Note that this is also driven, at least in part, by the scatter induced by the presence of carbon.

[17] Note that many of the literature stars with which we compare do not have published estimates of [C/Fe], so there no doubt exist more CEMP stars in our sample than shown in the figure, in particular among the EMP stars.

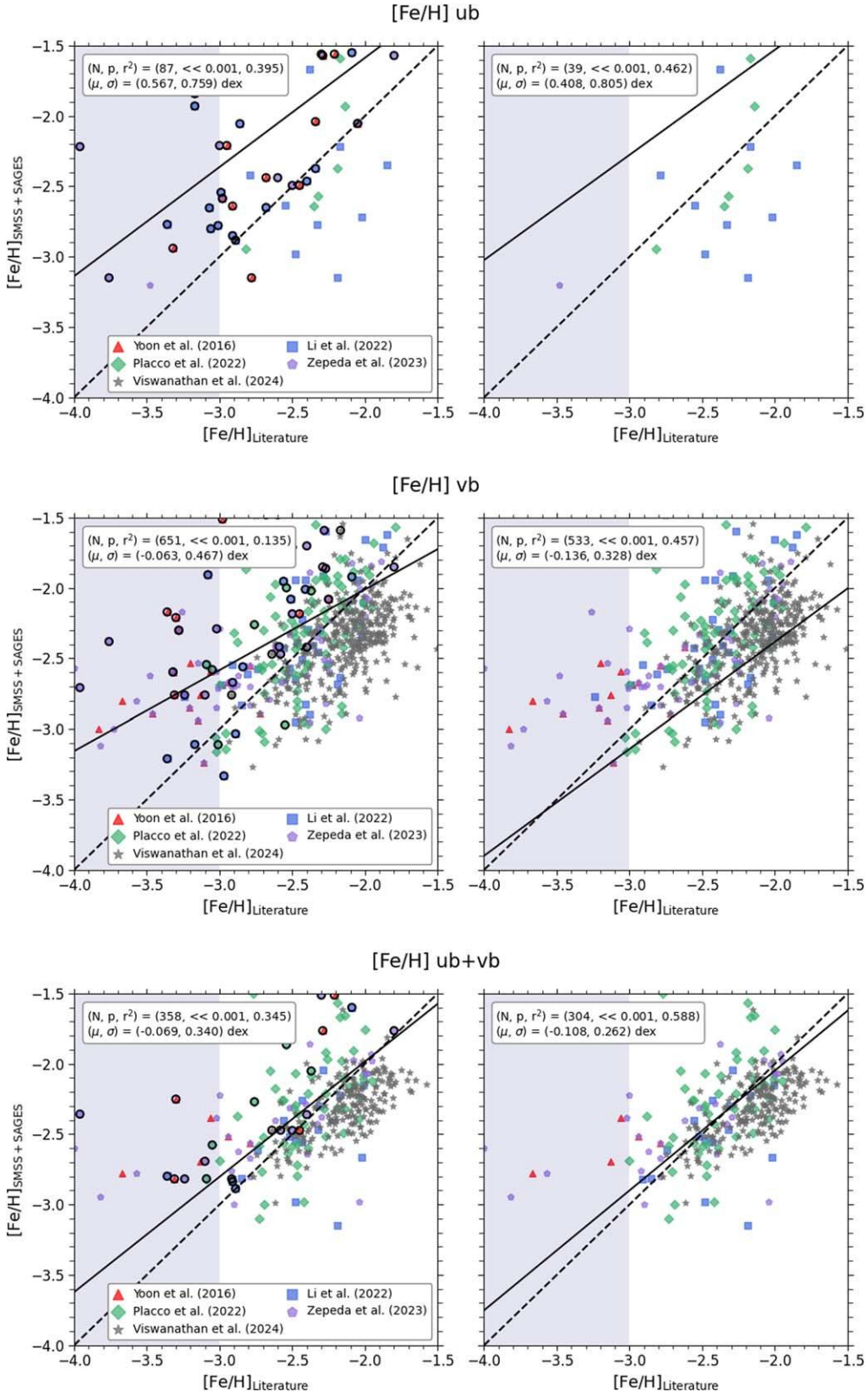

Figure A1. Left column: comparison of the combined SMSS/SAGES photometric-metallicity estimates and spectroscopic metallicities for VMP/EMP stars, based on cross-matches to medium/high-resolution spectroscopic samples with available [Fe/H] and [C/Fe]. The stars from Yoon et al. (2016), Li et al. (2022a), Placco et al. (2022), Zepeda et al. (2023), and Viswanathan et al. (2024) are shown as red triangles, blue squares, green diamonds, purple pentagons, and gray stars, respectively. The black circles indicate carbon-enhanced metal-poor (CEMP) stars that satisfy [C/Fe] $> +0.7$. Note that for our present purpose we employ the "as-observed" [C/Fe], without applying evolutionary corrections (e.g., from Placco et al. 2014). The black solid line is a linear regression line for all metallicity regions except for the range $[\mathrm{Fe/H}]_{\mathrm{Literature}} \leqslant -3$, a light-blue shaded region, and the dashed line represents a one-to-one line. The legends in each panel indicate the number of matching stars (N), the p-value, and the r^2 value in the Pearson correlation analysis, as well as the biweight location (μ) and scale (σ) of the metallicity residuals. Right column: comparison with the same spectroscopic catalogs, but excluding (recognized) CEMP stars. From top to bottom, the panels indicate matches for stars with metallicities based on the calibrated $u - G_{\mathrm{BP}}$ colors, the $v - G_{\mathrm{BP}}$ colors, and, when available, an average of both of these colors (Huang et al. 2022, 2023).

ORCID iDs

Jihye Hong https://orcid.org/0000-0002-2453-0853
Timothy C. Beers https://orcid.org/0000-0003-4573-6233
Young Sun Lee https://orcid.org/0000-0001-5297-4518
Yang Huang https://orcid.org/0000-0003-3250-2876
Yutaka Hirai https://orcid.org/0000-0002-5661-033X
Jonathan Cabrera Garcia https://orcid.org/0009-0006-7257-913X
Derek Shank https://orcid.org/0000-0001-9723-6121
Shuai Xu https://orcid.org/0000-0003-3535-504X
Haibo Yuan https://orcid.org/0000-0003-2471-2363
Mohammad K. Mardini https://orcid.org/0000-0001-9178-3992
Thomas Catapano https://orcid.org/0000-0001-9012-8320
Gang Zhao https://orcid.org/0000-0002-8980-945X
Zhou Fan https://orcid.org/0000-0002-6790-2397
Jie Zheng https://orcid.org/0000-0001-6637-6973
Wei Wang https://orcid.org/0000-0002-9702-4441
Kefeng Tan https://orcid.org/0000-0003-0173-6397
Jingkun Zhao https://orcid.org/0000-0003-2868-8276
Chun Li https://orcid.org/0009-0000-4835-7525

References

An, D., & Beers, T. C. 2020, ApJ, 897, 39
An, D., & Beers, T. C. 2021a, ApJ, 907, 101
An, D., & Beers, T. C. 2021b, ApJ, 918, 74
An, D., Beers, T. C., Lee, Y. S., & Masseron, T. 2023, ApJ, 952, 66
Bailer-Jones, C. A. L., Rybizki, J., Fouesneau, M., Demleitner, M., & Andrae, R. 2021, AJ, 161, 147
Baumgardt, H., & Vasiliev, E. 2021, MNRAS, 505, 5957
Beers, T. C., & Christlieb, N. 2005, ARA&A, 43, 531
Beers, T. C., Flynn, K., & Gebhardt, K. 1990, AJ, 100, 32
Beers, T. C., Norris, J. E., Placco, V. M., et al. 2014, ApJ, 794, 58
Beers, T. C., Preston, G. W., & Shectman, S. A. 1985, AJ, 90, 2089
Beers, T. C., Preston, G. W., & Shectman, S. A. 1992, AJ, 103, 1987
Bellazzini, M., Massari, D., Ceccarelli, E., et al. 2024, A&A, 683, A136
Bellazzini, M., Massari, D., De Angeli, F., et al. 2023, A&A, 674, A194
Belokurov, V., Erkal, D., Evans, N. W., Koposov, S. E., & Deason, A. J. 2018, MNRAS, 478, 611
Bressan, A., Marigo, P., Girardi, L., et al. 2012, MNRAS, 427, 127
Carollo, D., Beers, T. C., Chiba, M., et al. 2010, in IAU Symp. 265, Chemical Abundances in the Universe: Connecting First Stars to Planets, ed. K. Cunha, M. Spite, & B. Barbuy (Cambridge: Cambridge Univ. Press), 267
Carollo, D., Beers, T. C., Lee, Y. S., et al. 2007, Natur, 450, 1020
Carollo, D., Chiba, M., Ishigaki, M., et al. 2019, ApJ, 887, 22
Carollo, D., Christlieb, N., Tissera, P. B., & Sillero, E. 2023, ApJ, 946, 99
Carter, C., Conroy, C., Zaritsky, D., et al. 2021, ApJ, 908, 208
Cenarro, A. J., Moles, M., Cristóbal-Hornillos, D., et al. 2019, A&A, 622, A176
Chambers, K. C., Magnier, E. A., Metcalfe, N., et al. 2016, arXiv:1612.05560
Christlieb, N. 2003, RvMA, 16, 191
Conroy, C., Naidu, R. P., Zaritsky, D., et al. 2019, ApJ, 887, 237
Cordoni, G., Da Costa, G. S., Yong, D., et al. 2021, MNRAS, 503, 2539
De Silva, G. M., Freeman, K. C., Bland-Hawthorn, J., et al. 2015, MNRAS, 449, 2604
Deng, L.-C., Newberg, H. J., Liu, C., et al. 2012, RAA, 12, 735
Di Matteo, P., Spite, M., Haywood, M., et al. 2020, A&A, 636, A115
Fan, Z., Zhao, G., Wang, W., et al. 2023, ApJS, 268, 9
Feltzing, S., & Feuillet, D. 2023, ApJ, 953, 143
Fernández-Alvar, E., Kordopatis, G., Hill, V., et al. 2021, MNRAS, 508, 1509
Gaia Collaboration, Montegriffo, P., Bellazzini, M., et al. 2023, A&A, 674, A33
Gilmore, G., Randich, S., Worley, C. C., et al. 2022, A&A, 666, A120
GRAVITY Collaboration, Abuter, R., Amorim, A., et al. 2020, A&A, 636, L5
Harris, W. E. 2010, arXiv:1012.3224
Haywood, M., Di Matteo, P., Lehnert, M. D., et al. 2018, ApJ, 863, 113
Helmi, A., Babusiaux, C., Koppelman, H. H., et al. 2018, Natur, 563, 85
Hirai, Y., Beers, T. C., Chiba, M., et al. 2022, MNRAS, 517, 4856
Huang, Y., Beers, T. C., Wolf, C., et al. 2022, ApJ, 925, 164
Huang, Y., Beers, T. C., Yuan, H., et al. 2023, ApJ, 957, 65
Huang, Y., Liu, X. W., Yuan, H. B., et al. 2015, MNRAS, 454, 2863
Huang, Y., Yuan, H., Li, C., et al. 2021, ApJ, 907, 68
Keller, S. C., Schmidt, B. P., Bessell, M. S., et al. 2007, PASA, 24, 1
Kim, Y. K., Lee, Y. S., Beers, T. C., & Koo, J.-R. 2021, ApJL, 911, L21
Koppelman, H. H., Hagen, J. H. J., & Helmi, A. 2021, A&A, 647, A37
Lee, A., Lee, Y. S., Kim, Y. K., Beers, T. C., & An, D. 2023, ApJ, 945, 56
Li, H., Aoki, W., Matsuno, T., et al. 2022a, ApJ, 931, 147
Li, T. S., Ji, A. P., Pace, A. B., et al. 2022b, ApJ, 928, 30
Limberg, G., Santucci, R. M., Rossi, S., et al. 2021, ApJ, 913, 11
Luo, A. L., Zhao, Y.-H., Zhao, G., et al. 2015, RAA, 15, 1095
Majewski, S. R., Schiavon, R. P., Frinchaboy, P. M., et al. 2017, AJ, 154, 94
Mardini, M. K., Frebel, A., Chiti, A., et al. 2022a, ApJ, 936, 78
Mardini, M. K., Frebel, A., & Chiti, A. 2024, MNRAS, 529, L60
Mardini, M. K., Frebel, A., Ezzeddine, R., et al. 2022b, MNRAS, 517, 3993
Marigo, P., Girardi, L., Bressan, A., et al. 2017, ApJ, 835, 77
McMillan, P. J. 2017, MNRAS, 465, 76
Mendes de Oliveira, C., Ribeiro, T., Schoenell, W., et al. 2019, MNRAS, 489, 241
Norris, J., Bessell, M. S., & Pickles, A. J. 1985, ApJS, 58, 463
Onken, C. A., Wolf, C., Bessell, M. S., et al. 2019, PASA, 36, e033
Placco, V. M., Almeida-Fernandes, F., Arentsen, A., et al. 2022, ApJS, 262, 8
Placco, V. M., Frebel, A., Beers, T. C., & Stancliffe, R. J. 2014, ApJ, 797, 21
Reid, M. J., & Brunthaler, A. 2020, ApJ, 892, 39
Rockosi, C. M., Lee, Y. S., Morrison, H. L., et al. 2022, ApJS, 259, 60
Rybizki, J., Demleitner, M., Fouesneau, M., et al. 2018, PASP, 130, 074101
Santistevan, I. B., Wetzel, A., Sanderson, R. E., et al. 2021, MNRAS, 505, 921
Schlaufman, K. C., Thompson, I. B., & Casey, A. R. 2018, ApJ, 867, 98
Schlegel, D. J., Finkbeiner, D. P., & Davis, M. 1998, ApJ, 500, 525
Schönrich, R., Binney, J., & Dehnen, W. 2010, MNRAS, 403, 1829
Schuster, W. J., Moreno, E., Nissen, P. E., & Pichardo, B. 2012, A&A, 538, A21
Sestito, F., Buck, T., Starkenburg, E., et al. 2021, MNRAS, 500, 3750
Sestito, F., Martin, N., & Starkenburg, E. 2019, 53rd ESLAB Symp.: The Gaia Universe (Noordwijk: ESA), 47
Sestito, F., Martin, N. F., Starkenburg, E., et al. 2020, MNRAS, 497, L7
Shank, D., Komater, D., Beers, T. C., Placco, V. M., & Huang, Y. 2022, ApJS, 261, 19
Sotillo-Ramos, D., Bergemann, M., Friske, J. K. S., & Pillepich, A. 2023, MNRAS, 525, L105
Starkenburg, E., Martin, N., Youakim, K., et al. 2017, MNRAS, 471, 2587
Steinmetz, M., Zwitter, T., Siebert, A., et al. 2006, AJ, 132, 1645
Vasiliev, E. 2019, MNRAS, 482, 1525
Venn, K. A., Kielty, C. L., Sestito, F., et al. 2020, MNRAS, 492, 3241
Viswanathan, A., Starkenburg, E., Matsuno, T., et al. 2024, A&A, 683, L11
Xu, S., Yuan, H., Niu, Z., et al. 2022, ApJS, 258, 44
Yanny, B., Rockosi, C., Newberg, H. J., et al. 2009, AJ, 137, 4377
Yoon, J., Beers, T. C., Placco, V. M., et al. 2016, ApJ, 833, 20
York, D. G., Adelman, J., Anderson, E. J. J., et al. 2000, AJ, 120, 1579
Yuan, H., Liu, X., Xiang, M., Huang, Y., & Chen, B. 2015, ApJ, 803, 13
Zepeda, J., Beers, T. C., Placco, V. M., et al. 2023, ApJ, 947, 23
Zhao, G., Zhao, Y.-H., Chu, Y.-Q., Jing, Y.-P., & Deng, L.-C. 2012, RAA, 12, 723
Zheng, J., Zhao, G., Wang, W., et al. 2018, RAA, 18, 147